UNIVERSITY OF HELSINKI REPORT SERIES IN PHYSICS

HU-P- D265

Modification of bare and functionalized Au(111) surfaces and ferromagnetism of Au and Pd nanoclusters

Annika Venäläinen

Division of Materials Physics
Department of Physics
Faculty of Science
University of Helsinki
Helsingfors, Finland

ACADEMIC DISSERTATION

To be presented, with the permission of the Faculty of Science of the University of Helsinki, for public criticism in Auditorium E204 of the Department of Physics (Physicum) on the 21st of December 2018 at noon.

HELSINGFORS 2018

ISBN 978-951-51-2797-6 (printed version)
ISSN 0356-0961
Helsingfors 2018
Unigrafia

ISBN 978-951-51-2798-3 (PDF version)
http://ethesis.helsinki.fi/
Helsingfors 2018
Electronic Publications @ University of Helsinki

Annika Venäläinen, **Modification of bare and functionalized Au(111) surfaces and ferromagnetism of Au and Pd nanoclusters**, University of Helsinki, 2018, 45 p. + appendices, Report Series in Physics HU-P-D265, ISSN 0356-0961, ISBN 978-951-51-2797-6 (printed version), ISBN 978-951-51-2798-3 (PDF version)

Abstract

The purpose of this thesis is to provide a better understanding of the properties of surfaces covered by self-assembled monolayers (SAMs) as well as the magnetic properties of interacting nanoclusters of gold and palladium. Surfaces covered by SAMs were studied by investigating their possible metallization as well as the morphological changes in bare and SAM covered Au(111) surfaces induced by Ar irradiation. The ferromagnetism in bare Au and Pd nanoagglomerates produced by nanocluster deposition was also investigated.

SAMs used for this thesis are dodecanethiols (DDT, $CH_3(CH_2)_{11}SH$) for the study on Ar ion induced morphological effects, as well as 4-mercaptopyridine (4-MPy) and two different kinds of dithiocarbamates (DTCs, R_2NCS_2) for the metallization study. The Au and Pd clusters were generated using a gas aggregation source in the low energy-range. Surface morphologies were studied by the use of scanning tunnelling microscopy (STM), transmission electron microscopy (TEM) and atom force microscopy (AFM). X-ray photoelectron spectroscopy (XPS) was used to determine the chemical compositions of surfaces, whereas a superconducting interference device (SQUID) was utilized for magnetization measurements.

Our results show that DDT covered surfaces are more susceptible for irradiation-induced surface morphology changes than the unmodified Au surfaces. Flame-annealing of a Au(111) surface prior to ion bombardment is also found to be more susceptible to irradiation-induced surface defects. Based on our results it also seems that SAMs of DDT, 4-MPy, DTC, and DTC2 are impenetrable for Pd clusters deposited at thermal energies.

For assemblies of bare Au nanoclusters we present ferro- and superparamagnetic behaviour dependent on the interactions between particles. The enhanced surface-to-volume atomic ratio is found to favour ferromagnetism in the case of bare Au nanoparticles. For palladium nanocluster thin films we show that the ferromagnetic behaviour is highly dependent on the growth mode and film thickness, as these cause variations in the Pd cluster structures and resulting film morphologies.

Contents

Common abbreviations

4-MPy	4-mercaptopyridine
AFM	atom force microscopy
DDT	1-dodecanethiol
DTC	dithiocarbamate
DTC2	diethylditiocarbamate
FC	field-cooled
HR	high resolution
MNP	magnetic nanoparticle
NP	nanoparticle
SAM	self-assembled monolayer
SPM	superparamagnetism
SPM	scanning probe microscopy
STM	scanning tunnelling microscopy
SQUID	superconducting quantum interference device
TEM	transmission electron microscopy
UHV	ultra high vacuum
XPS	x-ray photoelectron spectroscopy
ZFC	zero field cooled

Chapter 1

Introduction

In nanoscience, objects and systems in which at least one dimension is in the range of 1-100 nm, are studied. This means that the objects are smaller than structures produced for microtechnologies, but larger than atoms and small molecules. The size of an object defines the physical properties of materials. As the size is reduced to the nanoscale the objects can exhibit new interesting and useful physical behaviour [1].

Already in ancient times gold nanoparticles were used to color glass, however, without the scientific understanding of today [2]. Probably the oldest and best known example of effects induced by nanoparticles, is the Lycurgus Cup, a Roman goblet from the 4th Century [3]. The glass cup appears opaque pea-green when it reflects light and deep wine-red as light is transmitted. Uncovering the secret behind the color took researchers over 20 years [4]. In 1962 it was uncovered that the optical effects were due to the presence of minute amounts of gold and silver in the glass, however the techniques available at the time, e.g. scanning electron microscope (SEM), were not able to reach the acquired resolutions, needed for more detailed analysis. In the late 1980s transmission electron microscopy (TEM) however enabled the researchers to show that the nanoparticles are silver-gold alloys, with a ratio of 7:3, containing an addition of 10% copper [4, 5]. Nowadays it is widely known that the colour of an object or liquid can be altered by using nanoclusters of different size and form and by varying the medium.

A nanocluster is an aggregate of a countable number of particles. Countable number being $2 - 10^n$, where $n \leq 7$, and particles being atoms or molecules [6]. Due to their size, nanoclusters can be considered to lay a bridge between small molecules and the solid state of matter. As the size is reduced from macro to micro, the surface to volume ratio will increase. This means that there will be increasingly higher percentages of surface atoms compared to the bulk ones, e.g. a cluster consisting of 10^6 atoms has 4% of the atoms on the surface, whereas the corresponding value is 40% for a cluster consisting of 10^3 atoms [7]. Consequently the optical, electronic and magnetic properties of nanoclusters will differ from those of bulk. One of the most interesting new findings, is the observation of magnetic properties in nanoscaled materials which are non-magnetic as bulk. This kind of behaviour has been observed in metal structures that typically are paramagnetic (e.g. Pd) and diamagnetic (Cu, Ag, Pt, Au), metal oxide nanoparticles and nanocrystalline films [8].

The deposition of clusters on surfaces creates a new class of systems highly relevant for practical applications, such as electronics, optics, biology, medicine and catalysis [9]. Thereby also the nano-scale properties and modifications of surfaces are of importance. E.g. by coating a surface with self-assembled monolayers (SAMs), organic assemblies formed onto surfaces, a surface can be stabilized and/or functionalized. SAMs are well-suited for studies in nanoscience as they link structures at the molecular level to phenomena at the macroscopic interface, e.g. wetting, friction and adhesion, and couple an external environment to the electronic and optical properties of metallic structures [1].

Chapter 2

Purpose and structure of this study

The purpose of this thesis is to provide a better understanding of the properties of surfaces covered by self-assembled monolayers (SAMs) as well as the magnetic properties of interacting nanoclusters of gold and palladium. More specifically the thesis aims to assess the following points

- The morphological changes in bare and SAM covered Au(111) surfaces by Ar irradiation.
- The metallization of SAM covered surfaces by Pd nanocluster deposition.
- The ferromagnetism in bare Au and Pd nanoagglomerates produced by nanocluster deposition.

The thesis consists of this summary and four research publications published in peer-reviewed international journals. The publications in this thesis are referred to by bold-face Roman numerals. This summary consists of seven sections. In this section, the publications are summarized and the author's contribution explained. Section 3 provides an overview of nanoclusters and self-assembled monolayers. Section 4 provides an overview on magnetism related to this thesis. Section 5 outlines the various experimental techniques and procedures used in connection with the conducted research. Section 6 presents the main results and a discussion. Finally, a conclusions and outlooks are presented in section 7.

2.1 Summaries of the original publications

Publication I: Argon ion irradiation induced morphological instability of bare and thiol-functionalized Au(111) surfaces, Annika Venäläinen, Minna Räisänen, Benoit Marchand, Kenizhiro Mizohata and Jyrki Räisänen, *Physical Chemistry Chemical Physics* 17 (2015) 10838−10848.

In this publication, the changes in the morphology induced by Ar ion irradiation, of bare and 1-dodecantehiol (DDT) SAM covered Au(111) surfaces, were investigated. The changes of the surfaces were analysed by scanning tunnelling microscopy (STM) and X-ray photoelectron spectroscopy (XPS) measurements, while the ion charge, energy and fluency were varied. The impact of flame-annealing of the Au(111) surface on subsequent ion bombardment was also considered. In general the DDT covered surface seemed to be more susceptible for irradiation-induced surface morphology changes than the bare Au surface.

Publication II: Metallization of self-assembled organic monolayer surfaces by Pd nanocluster deposition, Annika Venäläinen, Kristoffer Meinander, Minna Räisänen, Vladimir Tuboltsev and Jyrki Räisänen, *Surface Science* 677 (2018) 68−77.

In this publication, the metallization of thiol functionalized Au(111) surfaces were investigated. Four different kinds of SAMs were characterized by STM, TEM and XPS techniques both before and after deposition of different amounts of preformed Pd clusters. The experimental results indicated that all of the studied SAMs are impenetrable for Pd clusters deposited at thermal energies.

Publication III: Ferromagnetism in bare gold nanoagglomerates produced by nanocluster deposition, Annika Venäläinen, Pasi Jalkanen, Vladimir Tuboltsev, Kristoffer Meinander, Alexander Savin and Jyrki Räisänen, *Journal of Magnetism and Magnetic Materials* 454 (2018) 57−60.

In this publication, the magnetic behaviour of assemblies of bare Au nanoclusters were investigated. The morphology of the samples was analysed by high-resolution transmission electron microscopy (HR-TEM) and atom force microscopy (AFM) micrographs. A superconducting quantum interference device (SQUID) was used to determine the hysteresis with temperature dependent saturation magnetization, remanence and coercivity, as well as the magnetization temperature dependence. The results demonstrate ferro- and superparamagnetic behaviour in assemblies of bare nanoclusters. The detected magnetization is caused by the interaction between the separate clusters exhibiting a core-shell structure and is dependent on the total amount of gold clusters confined in the samples.

Publication IV: Growth mode-dependent ferromagnetic properties of palladium nanoclusters, Annika Venäläinen, Pasi Jalkanen, Vladimir Tuboltsev, Alexander Savin and Jyrki Räisänen, *Journal of Applied Physics* 124, 033904 (2018) .

In this publication, the changes in ferromagnetic behaviour of bare Pd nanoclusters were investigated, with respect to range and degree of interactions, starting from a network of clusters evolving to a film with porous morphology. The varying morphology of the resulting Pd film with respect to thickness suggests that cluster size, deposition energy and substrate type are crucial for the resulting film magnetization. This is demonstrated by the characteristic ferromagnetic hysteresis with the temperature dependent saturation magnetization, remanence and coercivity of palladium nanocluster aggregates.

2.2 Author's contribution

For all the publications presented in this thesis the author has been involved in planning the work, performed the background research, coordinated the schedules, kept track of the progress, taken part in the analysis and interpretation of the results, and writing of the manuscripts.

For publication **I** the author took part in the making of the samples, the argon irradiations as well as the STM and XPS measurements. The author analysed the STM results using the scanning probe microscopy data analysis software Gwyddion. The author was also one of the main authors of the manuscript.

For publication **II** the author prepared part of the SAM samples and carried out all the of the cluster depositions and took part in the STM and XPS measurements. The author analysed all of the STM results with Gwyddion, and took part in interpreting the results together with the results gained from the XPS measurements. For the manuscript the author wrote the introduction and the STM part of the results and discussion.

For publication **III** the author took part in the cluster depositions and carried out the depositions for the AFM measurements. The author analysed all of the SQUID results using Origin, the TEM results using Gatan Microscopy Suite software and the AFM results using Gwyddion. The author also wrote the manuscript.

For publication **IV** the author took part in the cluster depositions. The author analysed all of the SQUID results using Origin and the TEM results using Gatan Microscopy Suite software, and was one of the main authors of the manuscript.

Chapter 3

Nanoclusters and self-assembled monolayers

3.1 Nanoclusters

Nanoclusters are of high scientific interest, as they are small agglomerates of atoms or molecules and can be formed from almost all of the elements in the periodic table. Their properties can easily be tuned by varying the size and changing the materials they are composed of.

For metals and semiconductors the reduced size will e.g. have electronic effects. Large metal clusters represent a bridge between the molecular and solid state, as they exhibit properties belonging to both categories. The band structure evolves with increasing particle size [2]. Figure 3.1 shows the size quantization effect responsible for transition between a bulk metal and a cluster. The continuous density of states in the valence and conduction bands of the bulk will split into discrete electron levels, and with decreasing particle size the spacing between these levels and the band gap will increase. When cluster size becomes of the same order of magnitude as the wavelengths of electrons, the semiclassical model is no longer sufficient to explain the behaviour of matter and quantum-mechanical treatment becomes necessary [10].

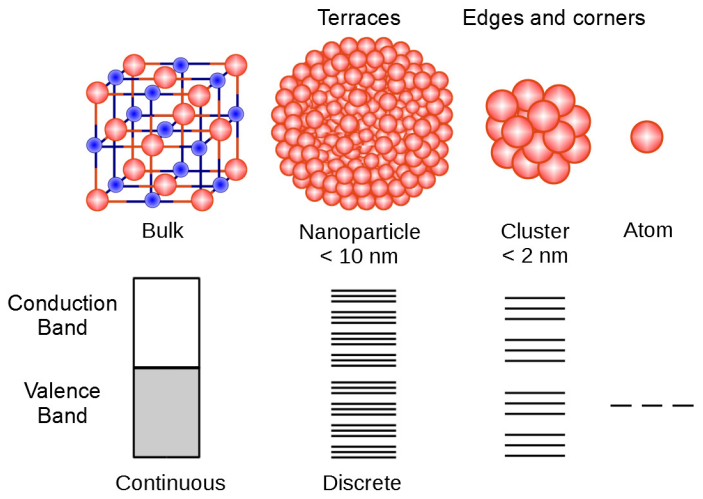

Figure 3.1: Schematic layout showing the evolution of matter from bulk to atom and the progression from metallic band structure to quantized electronic structure with the decreasing size.

Small metal nanoclusters and particles also show size-dependent properties in regard to melting temperature, as well as optical and magnetic properties [2]. As it recently has been observed that Pd and Au at the nanoscale show ferromagnetic properties, the ferromagnetism in nanoagglomerates of bare Au and Pd clusters were studied in publications **III** and **IV**. Palladium was also chosen for metallization of self-assembled monolayers in publication **II**, because Pd clusters have diverse applications e.g. as hydrogen sensors [11] and catalysts [12].

3.2 Self-assembled monolayers

Self-assembled monolayers (SAMs) are ordered molecular assemblies formed by the adsorption of an active surfactant on a solid surface, see Figure 3.2. The order in these layers is formed by a spontaneous chemical synthesis at the interface [13]. The monolayers are formed by immersing a substrate into a solution of a surface active material. A schematic diagram of an ideal SAM is shown in Figure 3.2. The main building block of a SAM is called a spacer, which is usually an alkane chain. The typical length of the spacer is $1-3$ nm, it provides a well-defined thickness, acts as a physical barrier, as well as alters the electronic conductivity and local optical properties of the monolayer. At one end of the chain there is a surface active head-group that binds the molecule to the substrate and at the other end there is a terminal functional group (interface group), which determines the characteristic properties of the surface [1, 13].

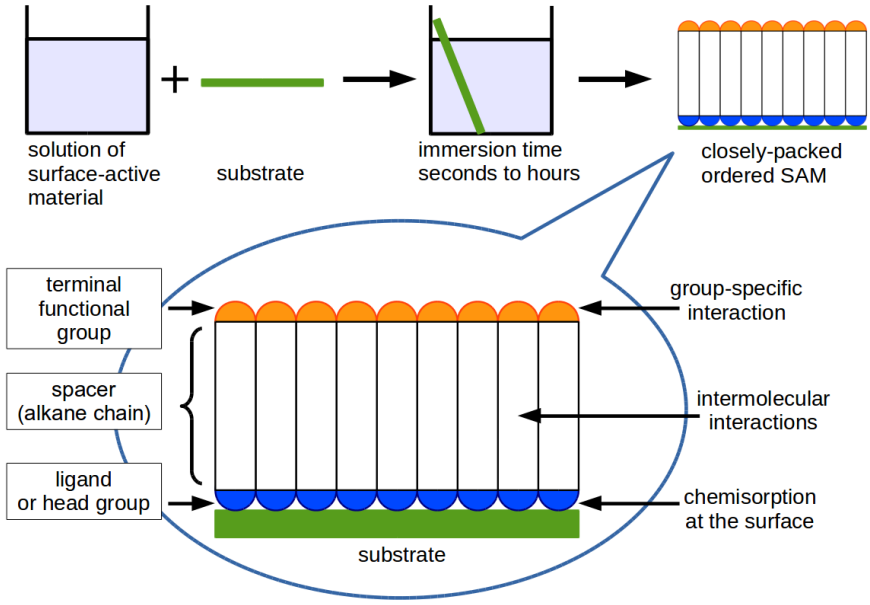

Figure 3.2: Illustration of the formation of SAMs. Image adapted from [13]

SAMs are highly useful for nanoscience and technology, especially as they are easy to prepare and do not require specialized equipment, e.g. ultra high vacuum in their preparation [1]. SAMs that have been used in this thesis are dodecanethiols (DDT, $CH_3(CH_2)_{11}SH$) in publication **I** and **II**, as well as 4-mercaptopyridine (4-MPy) and two different kinds of dithiocarbamates (DTCs, R_2NCS_2) in publication **II**. The schematic structures of the SAMs are shown in Figure 3.3.

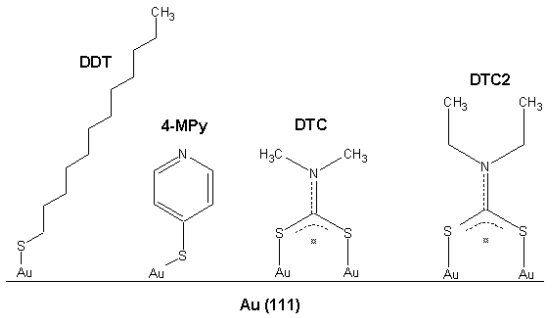

Figure 3.3: SAMs of n-dodecanethiol (DDT), 4-mercaptopyridine (4-MPy), dithiocarbamate (DTC) and diethyldithiocarbamate (DTC2) on Au(111) [14].

Alkanethiols ($CH_3CH_{n-1}SH$) are the most commonly used and studied molecules for SAMs. Thiols have a high affinity for the surface of noble and coinage metals, thereby they are ideal for the formation of well-defined organic surfaces with useful and highly alterable chemical functionalities, that are displayed at the interface [1, 15–17]. DDTs are alkanethiols, with an alkyl chain consisting of 11 carbon atoms, as the spacer, methyl (CH_3) as the functional group and a S-H as the head group.

DTCs on gold have been investigated both experimentally [18–21] and computationally [22], they form compact SAM layers, that are stable under various types of environmental stress and their ligands exhibit strong robustness [19, 20]. Although different in respect of rate and adsorption concentration, the surface coverage of DTCs on Au (111) is comparable to that of alkanethiols [21]. Under ambient conditions DTC SAMs on Au can be considered as a good alternative to alkanethiol-based SAMs [19, 21]. Like DDT, DTC and DTC2 are organic molecules terminated by methyl groups, see Figure 3.3. They do however have a resonant bi-denate structure that provides a molecule-metal coupling that is characteristically different compared to the one of thiols [20].

Pyridine is often used as "alligator clips" to firmly connect molecules to their respective metal electrodes, in the same manner as functional terminal groups in thiols [23]. Short aromatic thiolate SAMs, such as 4-MPy also show structural and conductive properties and are promising candidates for exploratory applications [24, 25]. 4-MPy consists of an aromatic ring, where one of the carbon atoms in the ring has been replaced by a nitrogen atom, see Figure 3.3. A 4-MPy covered surface will result

in an interface where nitrogen is situated at the topmost layer, which has shown to be one of the key factors in successful Pd-metallization [23, 26–31].

3.3 Nanocluster interaction with surfaces

When a cluster-surface collision is described a variety of different phenomena needs to be taken into account. The collision itself lasts for several picoseconds while the evolution of the cluster-surface system (e.g. evaporation, diffusion and aggregation) can last from hours to days [32]. When a cluster first comes into contact with a surface the front atoms of the cluster collide with the substrate atoms and are abruptly stopped. As the cluster atoms further away still have their initial velocity they will pile up and collide with the front atoms. Due to this compression the potential energy and internal kinetic energy of both cluster and surface will increase and heating will occur [32].

The outcome of a cluster-surface collision process varies depending on parameters such as cluster size (N), binding (cohesive) energy of the cluster and surface, bonds formed between cluster and surface atoms, impact energy (E_0), impact angle, charge state of the particle as well as the temperature of the cluster and surface [32]. A schematic figure of the fundamental processes that occur as a cluster interacts with a surface is shown in Figure 3.4.

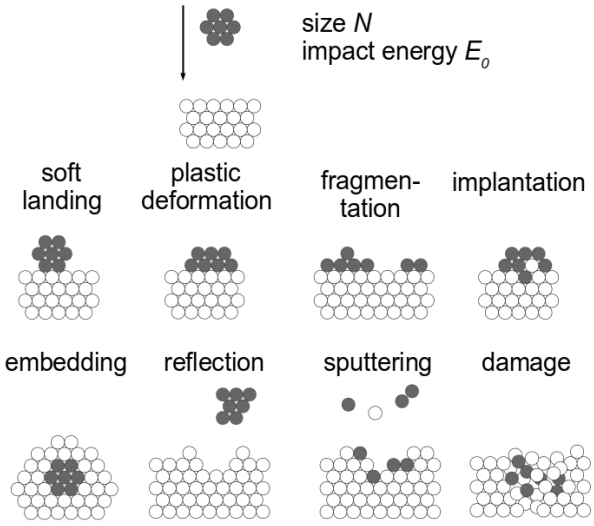

Figure 3.4: The fundamental processes occurring as a cluster interacts with a surface. Image adapted from [32].

Depending on the energy of the incoming cluster, the cluster-surface processes vary. They rarely occur separately but coexist. With increasing energy the deformation of the cluster and surface will increase. The interaction is considered to be in the low-energy regime if the kinetic energy per atom E_{atom} is below the binding energy of the cluster constituents E_{bind}, typically < 1 eV/atom [9]. 1 eV is also considered to be the upper limit for soft landing [32]. When considering soft landing, the collision is elastic and the cluster will stick to its impact point and keep its identity. The cluster can however undergo plastic deformation if E_{atom} is close to E_{bind} or if the deposited cluster strongly interacts with the substrate atoms [9, 32].

When E_{atom} exceeds E_{bind} the impact is considered as high-energy. If E_{atom} is only slightly above E_{bind} the cluster will on impact undergo significant plastic deformation and only parts of it will fragment [9]. If the impact energy is further increased cluster decomposition and fragmentation will occur. The cluster fragments can be backscattered from the surface or implanted in the substrate. When the fragments are implanted in the surface it will result in intermixing of the cluster and substrate or the cluster can become completely buried in the solid [32]. At relatively high impact energies the impact of the cluster can lead to significant erosion such as sputtering of surface atoms, reflection of cluster and crater formations [9]. At high energies the damage can be seen as formation of vacancies, interstitials and completely amorphous zones in the substrate [32].

When clusters are deposited on solid or soft surfaces from the gas phase, they impact the surface with low kinetic energy, as they are rarely accelerated towards the surface [33]. After a cluster has been deposited on a surface it will interact with the surface and the surrounding clusters, thereby the final morphology of the surface will depend on the cluster and substrate materials, as well as on the temperature and surface of the substrate. At first when two clusters impinge, they will become immobile and start a new island. This is followed by nucleation and island growth, after which islands saturate while their size continues to increase [34]. The shape of the islands strongly depend on the way the particles interact, whether they stick together, coalesce, agglomerate, or whether defects and/or impurities are present. In the case of coalescence, particles will merge and form a single larger particle. Agglomeration, on the other hand, will immobilize particles and form ramified island, while still preserving the shapes of the individual clusters [9, 34].

In order to preserve the form of the clusters used for publications **II**− **IV** the clusters have been deposited from gas phase in the low-energy regime ($\leq$ 0.16 eV for Pd and $\leq$ 0.3 eV for Au) [33]. In the low energy regime the deposited clusters will form well developed branches and porous like morphology of the resulting sample. The clusters act as building blocks, softly landing on top of each other and undergoing minor agglomeration [9].

If a metal surface is coated by a self-assembled monolayer the interactions are different when clusters are deposited, as the bonds formed between the cluster atoms and the atoms in the topmost layer of the SAM become crucial. The energy needed to break a chemical bond is roughly around 1 eV, which is above the energies used for this theses [33]. Penetration is almost always present when soft matter is affected by clusters, either the clusters have been grown on the surface or they have been deposited. The interaction between a metal atom and a metal surface is only slightly influenced by a organic layer. The metal-metal interaction is almost in all cases stronger than any metal-organic interaction, because of this metal atoms and clusters usually diffuse through soft matter. The final configuration is not necessarily a metal/metal interface, metal atoms or clusters can also become incorporated in the soft matter layer. Typically metal atoms penetrate through a monolayer via structural defects and two-dimensional structures are formed at the SAM-substrate interface [33].

The aim for the study in publication **II** was to prepare structures where Pd clusters are immobilized on top of different SAMs to create a metal-SAM-metal structure. The formation of metallic contacts of this kind are important for e.g. electronic applications [28]. Gas-phase formed clusters were chosen for the metallization, in order to separate the process of cluster nucleation from the surface interaction and dynamics of the surface, and limit the possibility for single adatoms to penetrate through the organic SAM.

Chapter 4

Magnetism

The macroscopic magnetic properties of matter are a result of magnetic moments associated with individual electrons. Each electron in an atom has magnetic moments that originate from the electron's orbital motion around the nucleus and its spinning around its own axis (spin). The magnetic moment due to spin is equal to the magnetic moment due to orbital motion (in the first Bohr orbit) and is approximately expressed in terms of the Bohr magnetron μ_B, (μ_B= 9.23 $\times$ 10^{-24} Am^2). For each electron in an atom the spin magnetic moment is $\pm\mu_B$ (plus for spin up and minus for spin down). The contribution of the orbital magnetic moment is equal to $m_l\mu_B$, where m_l is the magnetic quantum number of the electron [35].

The net magnetic moment of an atom is the sum of the magnetic moment for each individual electron, thereby the orbital and spin moment of some electron pairs cancel each other out. If an atom has completely filled electron shells there will be a total cancellation of both orbital and spin moments. Depending on the way electron and atomic magnetic dipoles respond to the application of an externally applied magnetic field, they can be categorized as diamagnetic, paramagnetic, ferromagnetic and at the nanoscale also superparamagnetic, typical magnetization curves for these responses are shown in Figure 4.1 [35].

Both dia- and paramagnetic materials are considered to be non-magnetic, as they only exhibit magnetization in the presence of an external magnetic field. Diamagnetism is induced when the orbital motion of electrons is changed due to an applied magnetic field. In the absence of an external field no dipoles exist, but as an external field is applied dipoles are induced and align opposite to the field direction. In a paramagnetic material, each atom has a permanent dipole moment due to incomplete cancellation of electron spin and/or orbital magnetic moments. These atomic moments are randomly oriented in the absence of an external magnetic field. As an external magnetic field is applied the atomic moments align with the external field [35, 36].

Ferromagnetic materials on the other hand possess a permanent magnetic moment in the absence of an external magnetic field and have very large permanent magnetizations. Even in the absence of an external magnetic field, coupling interaction will cause the net spin magnetic moments of adjacent atoms to align with one another. The mutual spin alignment exists over relatively large volume regions of crystal and are called domains [35].

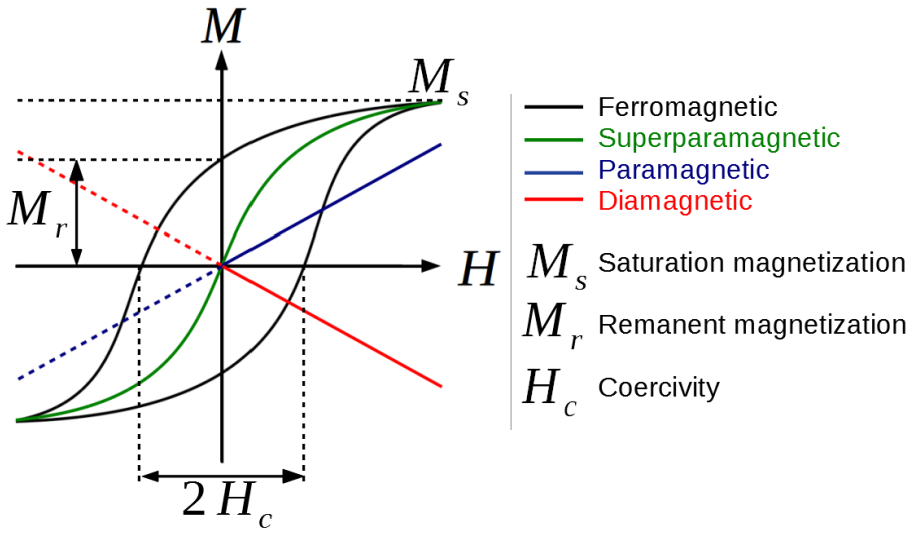

Figure 4.1: Typical magnetic behaviour (M) for a ferro-, super-, para- and diamagnet under the influence of an applied field (H). From the hysteresis loop for a ferromagnet the saturation (M_s), coercivity (H_c) and remanent magnetization (M_r) can be determined.

The maximum possible magnetization is called saturation magnetization M_s. For a ferromagnetic material, M_s represents the magnetization that results in all of the magnetic dipoles to be mutually aligned with an external field. The saturation magnetization is equal to the product of the net magnetic moments for all atoms present [36]. Since the atomic magnetic moments are free to rotate, the magnetic characteristics of a material are also temperature dependent. If the temperature is increased the thermal motion of the atoms will also increase, which in turn tends to randomize the directions of any moments that may be aligned. The saturation magnetization reaches its maximum at 0 K, as the thermal vibrations are at a minimum. With increasing temperature the saturation magnetization declines to a point, called the Curie temperature, T_C, at which M_s abruptly drops to zero [35].

A ferromagnetic material at temperature below T_C is composed of domains. The magnitude of the magnetization (M) of the entire solid is the vector sum of the magnetization of all the domains. If an external magnetic field (H) is applied on a ferromagnetic material, it will cause the domains having magnetization vectors in the direction of the applied field to grow at the expense of the domains in the opposite direction. When the total saturation is reached, the entire solid has become a single domain structure with the magnetization aligned with the external magnetic field [35].

The magnetization of a material (M) as a function of an applied field (H) is demonstrated by a hysteresis loop, see the magnetic behaviour (M) for a ferromagnetic material in Figure 4.1. After a ferromagnetic material has been magnetized in one direction, it will not relax back to zero magnetization, as the applied field is removed. In order to drive the magnetization back to zero, a field needs to be

applied in the opposite direction. If an alternating external field is applied on the ferromagnetic material, its magnetization will trace out a hysteresis loop. Hysteresis is the lack of re-traceability of the magnetization curve, which in turn is related to the existence of magnetic domains in the material. In order to change the domain structure in a ferromagnet (cause saturation) the existing domain walls need to move. The domain walls will resist this change, which can be seen as the lag of magnetization behind the applied field H and remanence M_r in the hysteresis curve. M_r is the induced magnetization that remains after an applied field has been removed. Coercivity H_c is the magnitude of an external field, that is needed to force the magnetization back to zero [35, 36].

4.1 Nanoparticle magnetism

Magnetic nanoparticles (MNPs) are nanoparticles (NPs) that show a response to an applied magnetic field. There are three main factors that influence the magnetic properties of MNPs and their ensembles: (1) the surface effects (2) interparticle interactions and (3) finite size effects [37].

4.1.1 Surface effects

At nanoscale the surface to volume ratio increases and thereby there is a larger number of atoms at the surface, along grain boundaries or particle/support interface than in the inner layers. Hence the surface will pay a significant contribution to the magnetization [38]. Surface effects result form the symmetry breaking of the crystal structure at the surface of a particle, oxidation, dangling bonds, existence of surfactants, surface strain or even different chemical and physical structures of internal core and surface shell parts of the nanoparticle [39].

The atoms at the surface have different environments than those in the core of a nanoparticle. Defects at the surface are not uncommon and they are usually a product of atomic vacancies, dangling bonds, lattice disorder or changes in atomic coordination. Due to these defects spins at the surface of NPs will be uncompensated disordered which in turn leads to surface magnetization [39]. It has been suggested that the total magnetization of a NP would be composed of two components; one component is related with the surface spins and the other with the core of the particle. Thereby the magnetization could be modelled via a core-shell magnetic model [38, 39].

4.1.2 Interaction effects

Depending on the nature of the matrix material and concentration of particles in an ensemble, various types of interparticle interactions can be present. The strength of these interactions determines the final magnetic structure. At a long range nanoparticles interact via dipolar forces, whereas exchange forces govern at the short range. The cross-over from dipolar-coupled to exchange-coupled behaviour occurs when the two types of interactions have comparable strengths. Interparticle interactions play

a crucial role on determining the response of an assembly of magnetic nanoparticles to an externally applied field. The interactions also influence the temperature dependence of the magnetic properties [37, 40].

Dipolar interaction summarizes the energy relationship between two magnetic moments. The interaction is long range and anisotropic in nature. The strength of the interaction depends on the separation of the dipoles as well as their mutual alignment. Depending on how de-localized the magnetic moments are and on the metallic/non-metallic properties of a solid, four different kinds of exchange couplings can be distinguished: direct exchange, superexchange, indirect exchange and itinerant exchange [41]. The relation between these couplings can be seen in Figure 4.2.

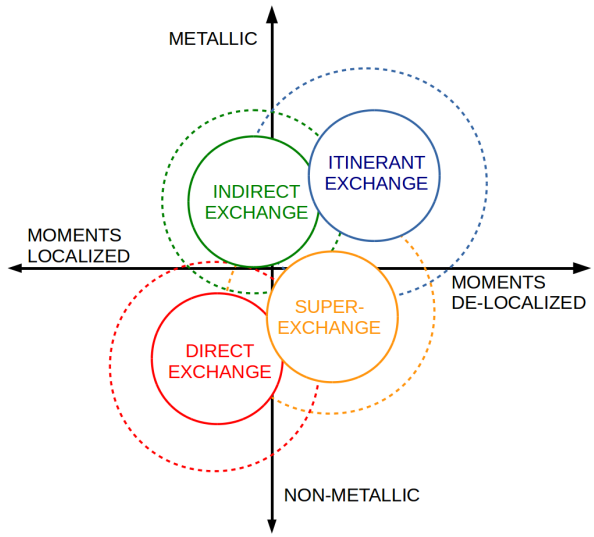

Figure 4.2: Relations between the exchange interactions. Double exchange is indicated as dashed circles. Image adapted from [41].

Direct exchange and superexchange apply for insulators. The direct exchange results from competition between kinetic energy (de-localization) and Coulomb repulsion. Direct exchange operates between moments, which are sufficiently close for their wave functions to overlap. This provides a strong coupling on a short range, which decreases rapidly as the moments are separated. Direct exchange interaction plays a leading role in the nanoparticle assemblies, as the surfaces of the particles often are in close contact [37]. Indirect exchange is the coupling between local magnetic moments of magnetic metals via conducting electrons, whereas itinerant exchange deals with the coupling between conducting electrons in metals. Additionally a double exchange needs to be added to all of the exchange couplings. This involves the coupling of two localized magnetic moments through an itinerant electron [41].

4.1.3 Size effects

As the size of a particle decreases, the domain walls will start to disappear, as they are energetically unfavourable, see Figure 4.3 [42]. This results in an increase of coercivity (H_c) until the particle size reaches a point, D_s, at which all the spins are aligned and a single domain is created [43]. In a single domain state the magnetization is uniform and behaves like a small permanent magnet. If a system consists of non-interacting (widely spaced) single domain particles the magnetic moments of the particles act independently. At this state the magnetization becomes unstable, as thermal agitation energy will overcome the magnetic anisotropy energy. When each particle behaves like a paramagnetic atom having a magnetic moment ($m \approx 10^3 - 10^5 \mu_B$) the phenomenon is called superparamagnetism [37, 43, 44].

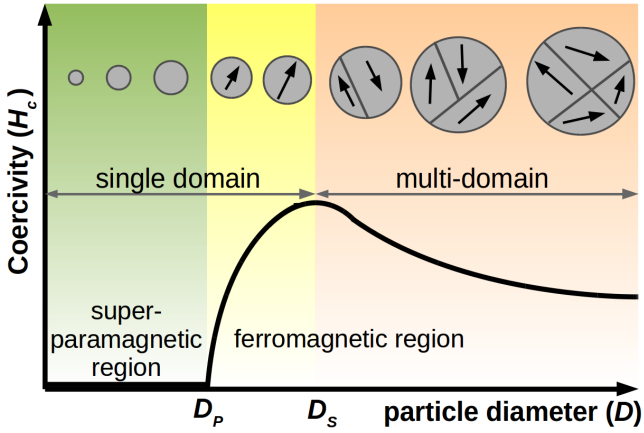

Figure 4.3: The influence of the particle size on the coercivity. Image adapted from [43].

4.1.4 Superparamagnetism

Superparamagnetism (SPM) refers to the influence of thermal energy on a ferromagnetic nanoparticle. Thermal energy causes the magnetic moments of the NPs in the superparamagnetic regime to fluctuate. This fluctuation will cause the magnetic moments to randomize unless a magnetic field is applied. SPM can be identified by characteristics of magnetization curves. A superparamagnet has no remanence or coercivity, see Figure 4.4a. Below a certain temperature, blocking temperature T_B, the ferromagnetic order will reappear [36, 45]. T_B is determined by measuring the magnetization as a function of temperature in a zero field cooled (ZFC) state, which is followed by a field cooled (FC) measurement, see Figure 4.4b.

In the ZFC-FC measurement the magnetization (M) is measured as a function of temperature under the influence of an external magnetic field (H). A sample is first cooled down in a zero field, after

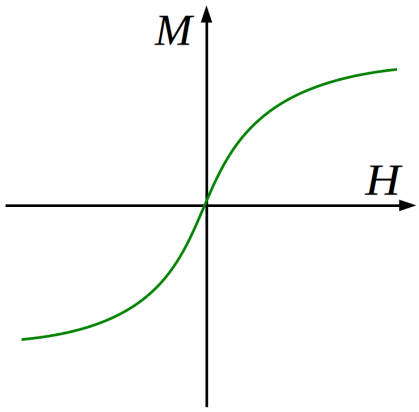

(a) Typical magnetization curve for a SPM as a function of an applied magnetic field.

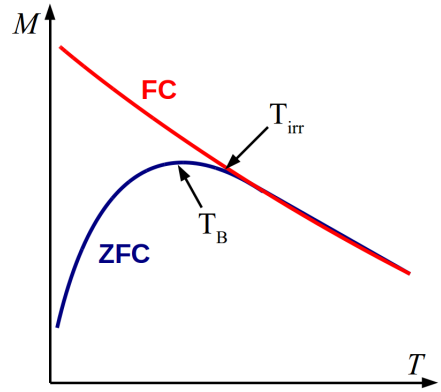

(b) Typical temperature dependent magnetization for a SPM.

Figure 4.4: Magnetization as a function (a) of applied field and (b) temperature. The zero field-cooled (ZFC) part in blue, field-cooled (FC) in red, the blocking, T_B, and irreversibility temperatures, T_{irr}, are indicated with arrows.

which an external magnetic field (H) is introduced. The magnetic field will cause the spins in the sample to reorientate away from the anisotropy axis into the direction of the magnetic field. After this the magnetization is measured with increasing temperature (ZFC part). The increased temperature assists the moments to reorientate in the direction of the magnetic field, which induces the measured magnetization [38]. The magnetization of a superparamagnetic material will pass through a maximum before it starts to reduce again at higher temperatures. The peak in the ZFC curve indicates the blocking temperature, T_B. Below the blocking temperature, the effects of thermal energy are diminished and ferromagnetic order will be regained. In the FC part the process is repeated, with the difference that the sample is cooled, in the presence of the same external field, applied during heating [36]. The temperature where ZFC and FC curves merge, and below which thermomagnetic irreversibility is shown ($M_{FC} > M_{ZFC}$), is called the irreversibility temperature, T_{irr} [46].

When an external magnetic field is applied to an assembly of superparamagnetic nanoparticles, their magnetic moments tend to align along the applied field. As superparamagnets don't show remanence or coercivity, it also means that the magnetization is reversible. In an ideal superparamagnetic system, the magnetization curve resembles an increasing s-shape, see Figure 4.4a, and can be expressed using a Langevin function [42, 47]:

$$M = M_0 L\left(\frac{\mu B}{k_B T}\right) = M_0 \left[\coth\left(\frac{\mu B}{k_B T}\right) - \frac{k_B T}{\mu B}\right]. \tag{4.1}$$

Chapter 5

Experimental techniques and procedures

5.1 Preparation of self-assembled monolayers

The SAMs that have been used in this thesis are dodecanethiols (DDT, $CH_3(CH_2)_{11}SH$) in publication **I** and **II**, as well as 4-mercaptopyridine (4-MPy) and two different kinds of dithiocarbamates (DTCs, R_2NCS_2) in publication **II**.

The SAMs of 4-MPy, DCT and DTC2 were prepared from their respective disulphide compounds, whereas DDT SAM was prepared from thiol. n-Dodecanethiol (DDT, $CH_3(CH_2)_{11}SH$, purity 98%), 4,4'-dithiodipyridine ($C_{10}H_8N_2S_2$, purity 98%), tetramethylthiuram disulfide (TMTD, $(CH_3)_2NCSS_2CSN(CH_3)_2$, purity 97%) and tetraethylthiuram disulfide (TETD $(CH_3CH_2)_2NCSS_2CSN(CH_3CH_2)_2$, purity $\geqslant$ 97%) were purchased from Sigma-Aldrich and used as received. All SAMs were prepared at room temperature (22 °C) on freshly flame-annealed Au(111) coated mica slides (300 nm Au, Georg Albert PVD). After immersions, the samples were rinsed with ethanol.

- DDT SAM: Au substrate was immersed in 1 mM ethanol solution of DDT for 24 h.
- 4-MPy SAM: Au substrate was immersed in 20 μM aqueous solution of 4,4'-dithiodipyridine for 15 min.
- DTC SAM: Au substrate was immersed in 1 mM solution of TMTD (ethanol:N,N'-dimethylformamide 1:1 v/v) for 24 h.
- DTC2 SAM: Au substrate was immersed in 1 mM solution of TETD (ethanol:N,N'-dimethylformamide 10:1 v/v) for 24 h.

5.2 Cluster deposition

The clusters used in publications **II**– **IV** were generated using the Facility for Nanocluster Deposition (FANADE) at the University of Helsinki. FANADE consists of a gas aggregation source connected to an ultra-high vacuum (UHV) chamber. A schematic overview of the instrument is shown in Figure 5.1.

The cluster material in a gas-aggregation cluster source is vaporized by magnetron sputtering [48]. In magnetron sputtering the target atoms are produced by bombarding a target (cathode) with ions that are generated in a glow discharge plasma, which is confined by a magnetic field [6, 49]. The sputtered

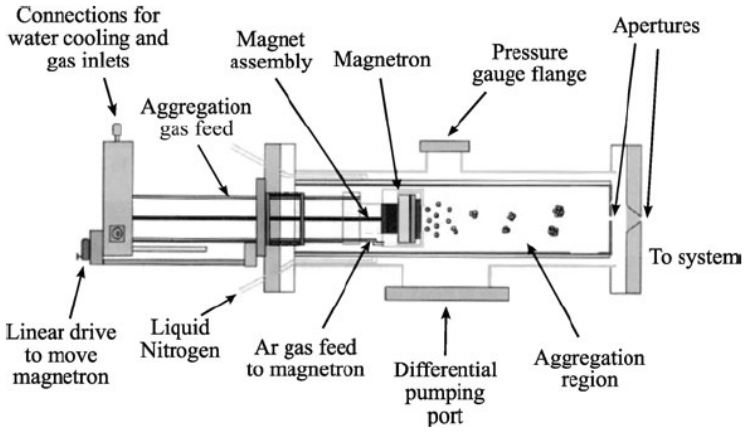

Figure 5.1: A schematic diagram of a condensation-cell-type cluster aggregation source.

atoms are neutrally charged and are unaffected by the magnetic trap, thereby the vaporized atoms can be swept into a condensation chamber (the aggregation region in Figure 5.1) by a flow of inert gas. In the condensation chamber the vapour cools down, due to collisions with the inert gas. After clusters condensate from the super-saturated vapour, they are swept out of the chamber by the inert gas flow and are deposited on a substrate. The size of the clusters generated can be varied by adjusting the length in which the clusters aggregate and by varying the power to the magnetron and the flow of the aggregation gas [50].

As the atoms exchange energy in collisions with the atoms in the inert gas the clusters eventually reach a velocity that is less than that of the streaming gas [51]. Thereby, the cluster velocity v_c can be approximated to be close to the expanding gas velocity, $v_c = v_{gas} = [2k_B T\gamma/(\gamma-1)m_{gas}]^{1/2}$, where γ is the heat capacity ratio for inert gas material, k_B is the Boltzmann constant, T the gas temperature and m_{gas} the atomic weight of the gas atoms [52]. Thus the kinetic energy E_{C} for the produced clusters can be approximated, based on $E_{\mathrm{C}} = 0.5NM_{\mathrm{C}}v_c^2$.

For the work in this thesis gas-phase formed clusters were chosen, as it allows to control the properties of the deposited clusters. For publications **III** and **IV** preformed clusters at the low energy-range were desired, as the aim was to investigate how the degree and range of interaction between the deposited clusters on a surface influences the magnetic behaviour. For publication **II** gas-phase formed clusters were chosen for the metallization of SAMs, in order to separate the process of cluster nucleation from the surface interaction and dynamics of the surface, and limit the possibility for single adatoms to penetrate through the organic SAM.

The palladium clusters for publications **II** and **IV** were produced with FANADE, charged with a Pd target of 99.99% purity. The clusters were agglomerated in argon gas and deposited in ultra-high vacuum at room temperature directly on the sample surfaces. For publication **III** the gold nanoclusters were produced with the same instrument, charged with a Au target of 99.999% purity, liquid nitrogen was employed as cooling, in order to produce larger clusters.

5.3 Ion irradiation

Ion irradiation is commonly used for surface modification. By varying the ion type, energy and fluency, the surface morphological changes generated can be controlled [53]. The use of low fluencies enables e.g. the creation of isolated defects such as vacancies and adatoms. An increased fluency may generate coarsening of the surface, and a longer bombardment time can lead to the development of a specific surface morphology [54, 55].

For publication **I** ion irradiation was employed in order to investigate the morphological changes in bare and thiol-functionalized Au(111) induced by argon ion irradiation. The argon ions were produced with a High Voltage Engineering 500 kV ion implanter at the University of Helsinki, where ions are produced by an cold cathode penning ion source (SO-60). The energies used for the normally-incident Ar ions were 10, 30 and 40 keV. The fluency during the Ar^{1+} irradiations of both bare Au(111) and DDT SAM/Au(111) surfaces were 10^{12}, 5×10^{12} and 10^{13} ions/cm^2. Bare Au(111) and DDT SAM/Au(111) surfaces were also irradiated with Ar^{4+} ions to the fluency of 10^{12} ions/cm^2 and 10^{13} ions/cm^2.

5.4 Surface characterization

5.4.1 Scanning Probe Microscopy

Scanning probe microscopy (SPM) is a branch of microscopy that forms images of surfaces using a physical probe that scans a sample. All probe microscopes have two features in common. Firstly, they consist of a tiny and sharp probe that is placed very close to a surface. The probe senses the surface by monitoring a distance sensitive interaction between the probe and the surface. Secondly the probe or the sample is scanned in a raster fashion, with almost an atomic accuracy. The variation in the investigated interaction is then translated to a topographic image of the surface. The two most commonly used SPMs are the Scanning Tunnelling Microscopy (STM) and Atomic Force Microscopy (AFM) [56, 57]. These are also the SPMs used in this thesis.

Scanning Tunnelling Microscopy

STM is an imaging technique, capable to an atomic scale resolution of an electrically conductive sample. On the left hand-side of figure 5.2 an overview of the working principle for a STM system can be seen. Under the optimal conditions it is possible to acquire three-dimensional (3D) images at near sub-atomic resolution. The operating principle is based on the quantum-mechanical phenomena of tunnelling current, where a sample and a sharp tip are held a few Ångströms apart and the current between them is measured [56, 57].

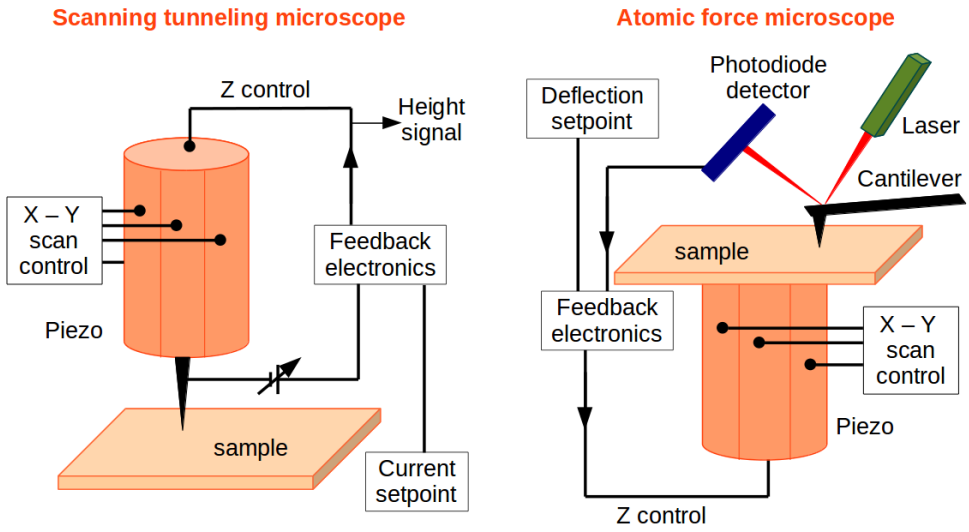

Figure 5.2: A schematic showing the basic setup for a STM (to the left) and for an AFM (to the right).

The tip (or the sample) is mounted on a piezoelectric scanner (with three perpendicular piezoelectric transducers:x-,y- and z piezo). As the tip is moved relative to the surface, changes in the tunnelling current represent a change in the separation distance [57, 58]. The measured tunnelling current is converted to a voltage by a current amplifier, which is then compared with a reference value. When the tip scans over the xy plane, a two-dimensional array of equilibrium z positions, representing the contour plot of the equal tunnelling-current surface, is obtained [58].

The STM characterizations for Publications **I** and **II** were performed using a Veeco Instrument Nano-Scope V-MultiMode scanning probe microscope in constant-current mode under ambient conditions, at the University of Helsinki. The STM tips were mechanically cut Pt/Ir (80:20) wires of 0.25 mm diameter. The acquired STM data were analysed using the SPM data analysis software Gwyddion [59].

Atom Force Microscopy

The operating principle of an atom force microscope is based on the ability to sense small forces. On the right hand-side of figure 5.2 an overview of the working principle for an AFM system can be seen. In an AFM, the probe tip is attached to a cantilever with a small spring constant. A forces acting on the probe tip deflect the cantilever and the tip displacement is proportional to the force between the surface and the tip. The resultant bending of the AFM cantilever is measured optically by the deflection of a reflected laser beam onto a split photodiode. The most important advantage that AFM has over STM is that the former is not limited to conducting samples, so materials can often be imaged "as is" with almost no sample preparation [56].

The AFM characterizations for Publication **III** were performed using a Veeco AutoProbe CP-Research atom force microscope, in tapping mode, under ambient conditions, at the University of Helsinki. A silicon cantilever was used with a tip radius > 20 nm. The acquired AFM data was analysed using the SPM data analysis software Gwyddion [59].

5.4.2 Transmission Electron Microscopy

In a transmission electron microscope a thin sample is irradiated with an electron beam, with uniform current density. An overview of the working principle for a TEM can be seen in Figure 5.3. Electrons are emitted with an electron gun. Condenser-lens systems enable variations in the illumination aperture and the beam can be focused and aligned to the sample using electromagnetic lenses. If the sample is electron dense, less electrons will penetrate. This will form an image of light areas where the electron beam has remained intact and dark areas where electrons have scattered. [57, 60].

The TEM characterizations for Publications **III** and **IV** were performed using a high-resolution TEM (JEOL JEM-200FS) at the Aalto University School of Science. The acquired TEM data were analysed using the Gatan DigitalMicrograph software.

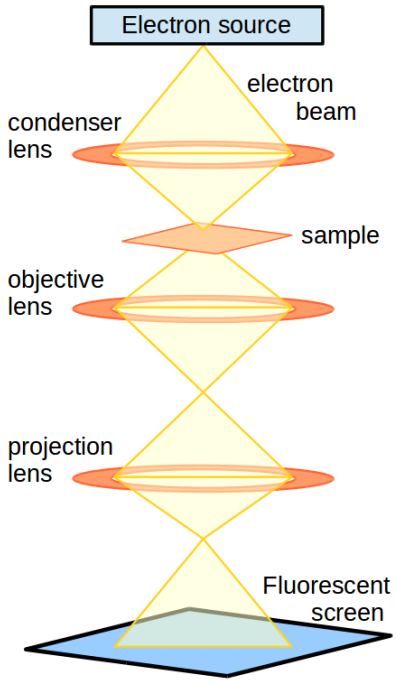

Figure 5.3: A schematic showing the basic components for a TEM.

5.4.3 X-ray Photoelectron Spectroscopy

XPS is a surface sensitive quantitative spectroscopic technique. XPS spectra are obtained by measuring the energy distribution of electrons ejected from a solid via irradiation by X-rays and the photoelectronic effect. The detected electrons contain information about the chemical oxidation state, electronic structure and the atomic composition of the studied substrate[61].

A schematic representation of a typical XPS setup is given in Figure 5.4. The basic operating principle is based on the interaction of an X-ray photon with a sample, which leads to the ejection of photoelectrons. The analysis is based on the determination of the kinetic energy of the outgoing electron, as the kinetic energy (E_{kin}) of the ejected photoelectron is related to the electron binding energy (E_B). The binding energy defines the element and atomic level from which the photolectron originates [62]. As the energy of the used X-ray with a particular wavelength is known (for Mg K_α X-rays, E_{photon}=1253.6 eV) and the emitted electrons kinetic energy is measured the electron binding energy can be determined for each of the emitted electrons based on, $E_B = E_{photon} - (E_{kin} + \phi)$, where ϕ is the work function for the spectrometer.

The XPS data for the work in this thesis was obtained using an Hiden Analytical SIMS/SNMS/XPS

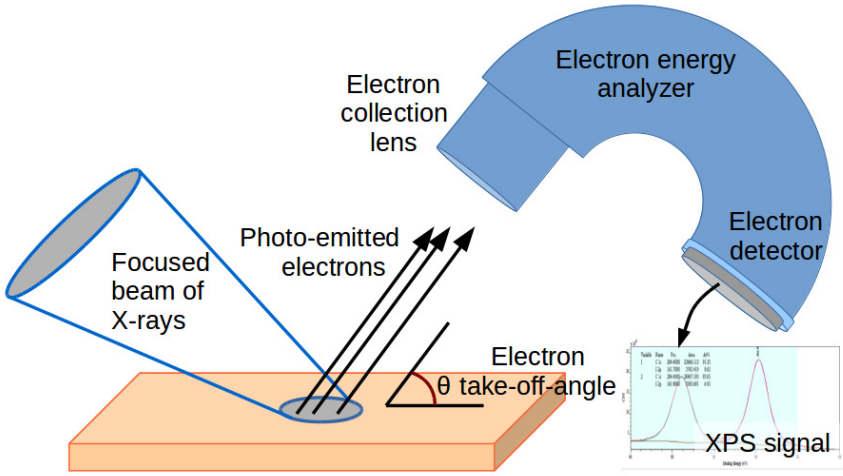

Figure 5.4: Schematic representation of a XPS setup.

system, equipped with an Mg K_α X-ray source (Omicron DAR 400), at the University of Helsinki. In publication **I**, the X-ray photoelectron spectroscopy technique was used to characterize the chemical and physical effect that argon ion irradiation induced on the samples. In publication **II**, the XPS technique was used to determine the composition and chemical state of the sample surfaces before and after Pd cluster deposition. The main results are outlined in section 6.

5.5 Magnetization measurement

The most sensitive magnetic flux detector is the superconducting quantum interference device (SQUID). The device operates at cryogenic temperatures with quantum-limited sensitivity. It uses the Josephson effect to measure extremely small variations in magnetic flux [63].

Typically a SQUID sensor consists of a superconducting loop which has one or more Josephson junctions, see Figure 5.5. The sensor's input coil is connected to a pickup coil inside a superconducting magnet. When a sample is moved inside the superconducting magnet and pickup coil it will induce a change in the current of the pickup coil, that in turn will induce a change in the magnetic flux from the input coil [64].

In the SQUID loop a bias current (I_b) is applied giving a operational point, that is midway between the superconducting and resistive behaviours. As a magnetic flux is inductively coupled into the SQUID loop a screening current is created. The screening current will increase or decrease the critical current I_c, of the Josephson junction, depending on the direction of the induced flux. I_b is fixed at a slightly

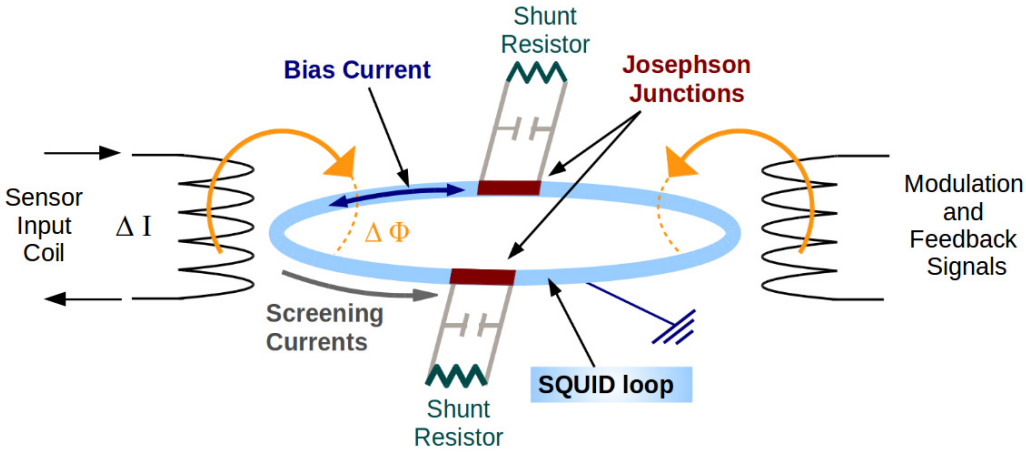

Figure 5.5: Schematic representation of a SQUID sensor. Image adapted from [64].

higher value than I_c, so that when an external magnetic flux ($\Phi_{ext} = B_{ext}A$) is coupled into the Josephson loop, the voltage will drop [64].

The magnetic flux through the loop is quantized. As the external flux increases (or decreases) the voltage will change periodically, where the period corresponds to one flux quantum Φ_0 (2.068×10^{-15}Wb). The variation of the flux by one quantum causes the current to change sign, thereby monitoring the change in voltage allows the determination of the magnetic flux that has been coupled into the SQUID loop and the magnetic moment can be measured [64, 65].

The SQUID measurements for Publications **III** and **VI** were performed using a Quantum Design MPMS-XL7 SQUID magnetometer at the Aalto University School of Science. The used nanoconducting solenoid provided a magnetic field up to 70 kOe at temperatures from 1.8 to 400 K. Before the actual SQUID measurements of the investigated nanoclusters, the background signal influenced by the template shape, local deformations, material defects and non-homogeneity was measured. This was done by measuring the template (without any depositions) with all of the experimental conditions exactly the same as during the actual measurements. The resulting data was then subtracted from the actual magnetization data measured from the clusters deposited on the templates. The results are outlined in section 6.3.

Chapter 6

Results and Discussion

6.1 Morphological changes in bare Au and SAM covered Au(111) surfaces by argon irradiation

Ar ion irradiation-induced changes in the morphology of bare Au(111) surfaces as well as surfaces covered by 1-dodecanethiol SAMs, were examined in publication **I**. The changes in the surface morphology were followed by STM and XPS measurements while varying the ion charge (Ar^{1+}, Ar^{4+}), energy ($10-40$ keV) and fluency ($10^{12}-10^{13}$ ions/cm^2). The impact of flame-annealing of the Au(111) surface prior to ion bombardment was also investigated.

Our study of Au(111) surfaces irradiated by Ar ions serves as control experiment for the irradiated DDT covered Au(111) surfaces. In spite of the fact, that gold is the most common substrate for SAMs, there are no previous systematic studies available, regarding the effects of ion bombardment on Au surfaces as a substrate for SAMs. The reports available in literature are found to be disconnected studies mainly concerning structures created by highly charged $Xe^{25+,44+}$ ions, with non-conclusive results [66–68].

The majority of studies available in the literature, concerning ion-SAM interactions report observations of the sputtered molecular and cluster ions and emission processes [69–71]. Only one previous study was found to concern the morphological modifications of SAM covered surfaces induced by ion interactions [72]. In that study DDT SAM covered Au(111) surfaces were irradiated by 14 keV argon ions with charge states of 7+ and 8+. The results obtained by STM and TOF-SIMS measurements led the authors to the conclude, that only minor surface defects which correspond to cleavage of the uppermost hydrogen atoms from the thiolate molecules, were induced by the used irradiation [72].

In publication **I** the impact of flame annealing of the Au(111) surface was investigated by irradiating a Au(111) substrate in as-received condition and another that had been flame-annealed. Both samples were irradiated by 40 keV Ar^+ to the fluency of 10^{13} ions/cm^2. STM characterization and subsequent data analysis of the samples clearly show irradiation-induced changes on their surface morphologies (Figure 6.1 a $-$ c). STM image of the surface prior the irradiation appears similar to that of the flame-annealed surface presented in Figure 6.1a. On the whole the STM data suggests that annealing of the substrate makes it more susceptible to irradiation-induced surface defects but no specific cause for

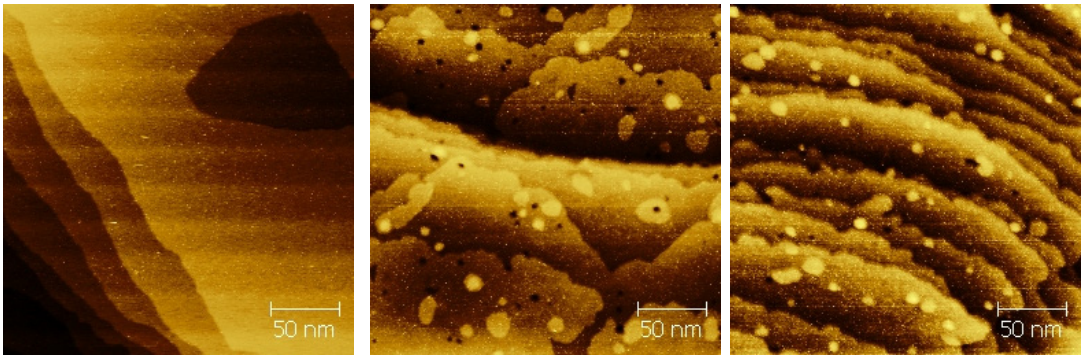

(a) Flame-annealed Au(111) surface prior to irradiation.

(b) Flame-annealed Au(111) surface after irradiation.

(c) Non-annealed Au(111) surface after irradiation.

Figure 6.1: Large-scale STM images of Au(111) prior and after 40 keV Ar^{+} to the fluency of 10^{13} ions/cm^2.

this can be pointed out. All of the subsequent experiments were carried out by using flame-annealed substrates, since they are more conventionally used.

The irradiation of bare Au(111) surfaces was found to generate Au vacancy and adatom islands and cause roughening of step edges. The ion energy and fluency had a large impact on the size and abundance of the islands caused by the irradiation as well as on the level of reconstruction on the step edges. The correlation between ion energy and fluency as well as the average projected surface area of vacancy and adatom islands of the irradiated Au(111) surface is shown in Figure 6.2 a.

For the SAM functionalized surface, the Au adatom islands were modified, step edges roughened and Au adatom islands were formed. The level of surface reconstruction also increased as a function of ion energy and fluency for the SAM functionalized surfaces. The surface modification occurs in such a way that the combined defect island surface areas are roughly the same before and after the irradiation. Surface reconstruction increases as a function of ion energy and fluency and the gold vacancy and adatom islands are on the average larger on the Ar^{4+} irradiation modified surfaces than on the Ar^{1+} modified surfaces. The correlations between ion energy, fluency and charge state, and the average projected surface area of vacancy and adatom islands of the irradiated DDT SAM covered Au(111) surface is shown in Figure 6.2 b. A more detailed analysis revealed that the thiolate molecules remained mostly closely-packed and in a standing-up orientation on the surface irradiated to the fluency of 10^{12} ions/cm^2 whereas irradiation to the fluency of 10^{13} ions/cm^2 resulted in their reduced surface coverage and flat-lying molecules.

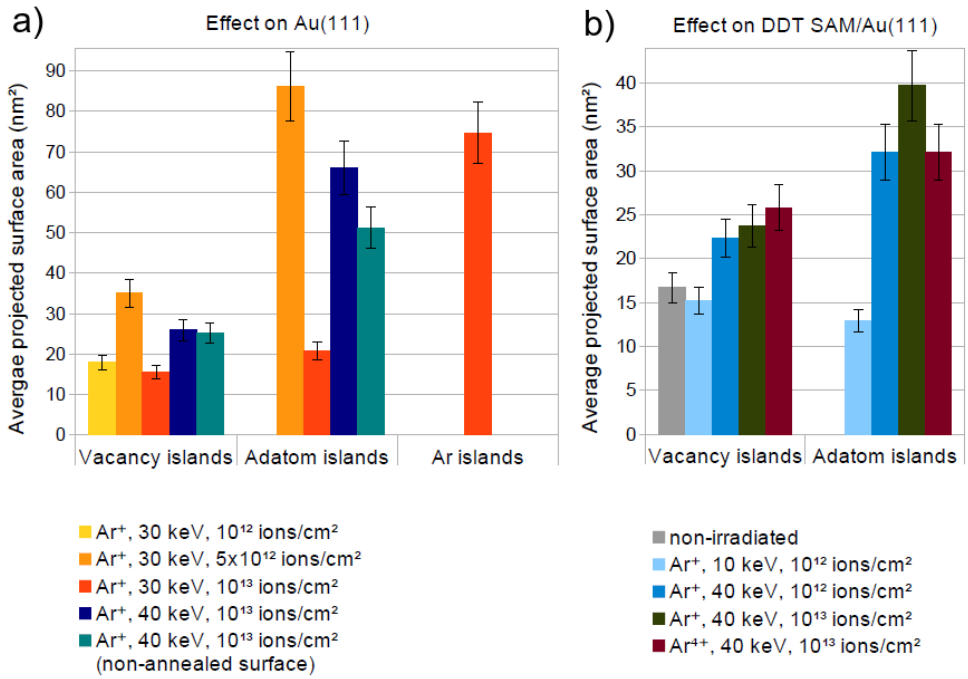

Figure 6.2: a) The correlations between ion energy and fluency, and the average projected surface area of vacancy and adatom islands of the irradiated Au(111) surfaces. b) The correlations between ion energy, fluency and charge state, and the average projected surface area of vacancy and adatom islands of the irradiated DDT SAM covered Au(111) surface. Note that no adatom islands were present in the non-irradiated sample. Reproduced from Ref. [73] with permission from the PCCP Owner Societies.

6.2 Metallization of SAMs by Pd nanocluster deposition

For publication **II** Au(111) surfaces were covered with four different SAMs (DDT, DTC, DTC2 and 4-MPy). The surfaces were uniformly deposited with Pd clusters for 15, 30, 45 and 60 s. The surface structures prior to and after Pd-metallization were studied using STM and XPS techniques. Publication **II** is a build-up on a previous study by our group, where morphologies of DDT SAM/Au(111) surfaces were investigated after gas phase deposition of gold and other coinage metal clusters [74, 75]. In this work the study was extended to the cluster deposition on different types of SAMs as such systematic studies have so far been lacking in the literature.

In most studies reported in the literature, metallization is achieved by vapour [76–79], electrochemical [29–31] or electroless deposition [76, 80–82]. The downside with the vapour deposition techniques is that they are based on separate atoms being deposited on the surface and then undergoing possible nucleation. Organometallic chemical vapour deposition has been used to deposit Au on SAMs [79] and pulsed laser deposition has been used to deposit patterns of Pt, Pd, Cu and Au on different SAMs

[76–78]. Electrochemical method on the other hand requires a precise potential control on samples, which is also a challenge for serial production of nanostructured molecular junctions. The drawbacks with electroless deposition is the involvement of solution electrochemistry as reducing agents for metallic adlayer formation, as well as the care required in choosing reducing agents in order to avoid impurities in the final deposit [82].

For the study in publication **II** Pd clusters were chosen for the metallization of SAMs, as Pd clusters show different possibilities in applications e.g. as hydrogen sensors [11] and catalysts [12]. To our knowledge there are no previous reports on gas-phase Pd clusters deposited on SAMs. In our study we have chosen to use gas-phase formed clusters, as the use of preformed clusters has the advantage of separating the process of cluster nucleation from surface interactions and dynamics on the surface.

In order to characterize the size distribution of the deposited Pd clusters TEM measurements were carried out. Figure 6.3 a) shows a typical TEM image from a 15 s Pd cluster deposition on a standard TEM-grid, while Figure 6.3 b) shows the radial size distribution of clusters for both 15 and 60 s Pd depositions. Diffusion and coalescence of the clusters determines the final cluster size distribution, this can be seen from the irregular shape of the upper cluster in the high-resolution inset (side length 10 nm) and the shift in the cluster size distributions going from 15 s to 60 s deposition. STM studies were conducted for bare and DDT, DTC and DTC2 SAM covered Au(111) surfaces before and after Pd cluster deposition. Typical STM images of the sample surfaces before and after Pd cluster deposition

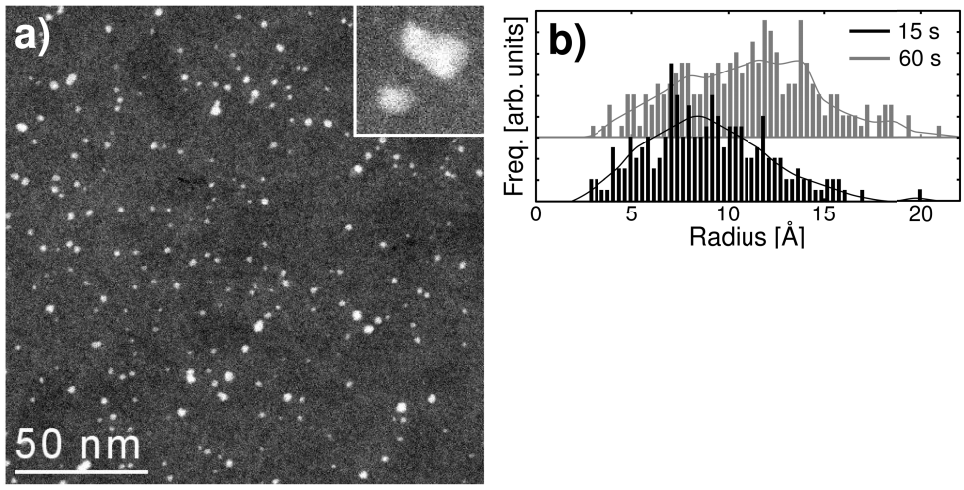

Figure 6.3: a) TEM image of Pd clusters deposited on a carbon coated TEM-grid. The inset in the top right corner (side length 10 nm) shows a magnification of an irregular cluster shape. The size distributions of cluster radii, as calculated from the cluster areas, is given in b) for 15 and 60 s of Pd cluster deposition, respectively [14].

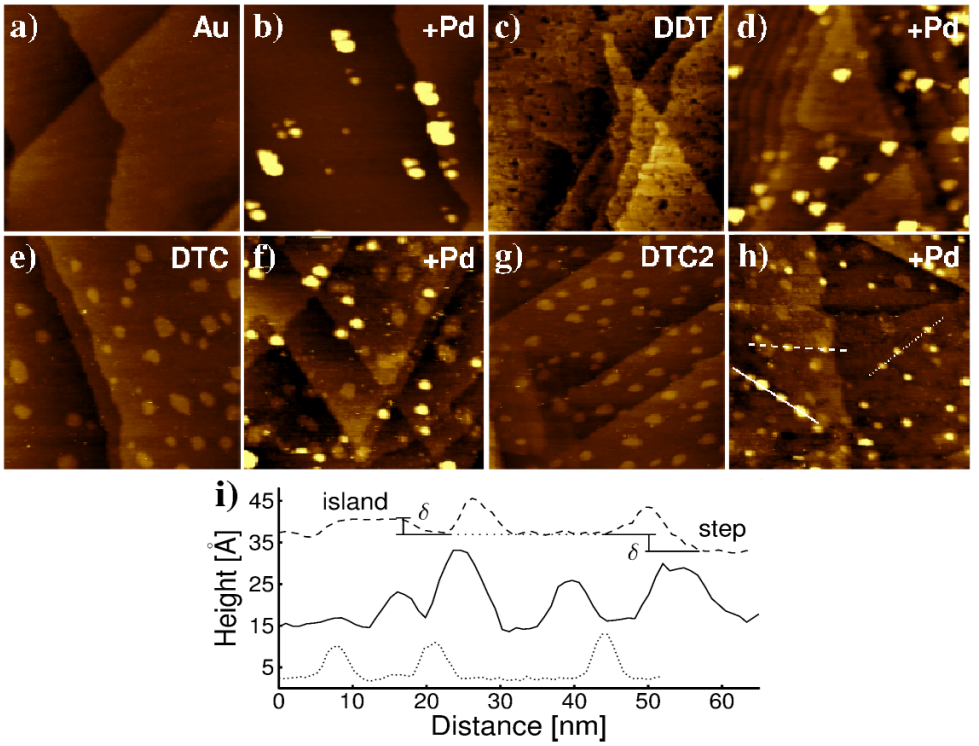

Figure 6.4: a)−h) STM images before and after Pd deposition on bare Au(111), DDT, DTC, and DTC2. Side lengths are 150 nm, height scale is 1.4 nm. Line profiles from h) are shown in i). $\delta = 0.24$ nm.

are shown in Figure 6.4. For 4-MPy we were not able to obtain good quality images, thereby the 4-MPy samples were only studied by XPS.

In all of the post-deposition STM images the Pd clusters can clearly be distinguished and a height distribution for the deposited clusters could be extracted, see histograms in Figure 6.5. The height distribution of Au islands on the DTC and DTC2 covered surfaces before and after Pd cluster deposition are presented in Figure 6.5 a). Figure 6.5 b) shows a comparison of the Pd cluster height distributions on Au(111), DDT, DTC and DTC2 covered surfaces.

From the histogram in Figure 6.5 a) it can be seen that the total amount of Au monolayer islands on DTC and DTC2 covered surfaces decreases as Pd clusters have been deposited. The more significant decrease of Au monolayers for DTC SAM, could be due to Au islands acting as pinning points for the clusters. The DTC also exhibits a broader distribution, with increased amount of larger clusters compared to DTC2. This would imply toward a more intense aggregation and diffusion of clusters on the DTC surface. According to previous studies DTC2 form more well-ordered monolayers than

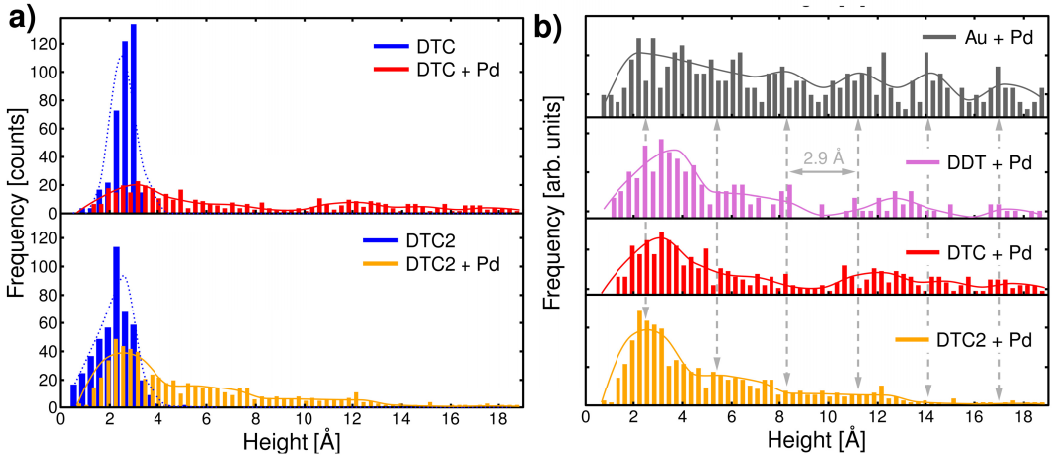

Figure 6.5: a) A comparison of measured heights from the DTC and DTC2 STM images before and after a 30 s Pd deposition. b) Distribution of cluster heights acquired by STM [14].

DTC [21, 83, 84], which could explain wherefore a larger amount of smaller gold islands are formed on the DTC2 surface, see Figure 6.5.

For the Pd cluster distribution on the bare Au surface it can be noted that there seems to be periodicity in the measured heights of ∼2.9 Å. Since Pd and Au are both FCC metals, they have a certain affinity for each other and can easily form alloys, therefore Pd clusters will align themselves in the [111] direction when they are deposited on Au(111) surfaces. The step height of a Pd(111) surface should be ∼ 2.3 Å, but due to oxidation there will be an increase of 18-30% in the step height, which would correspond to the observed periodicity of ∼ 2.9 Å [85]. A similar periodicity cannot however be seen for the Pd clusters deposited on the SAM covered surfaces, which would indicate that the Pd clusters have not penetrated through the organic layer and formed a single-atom thick interfacial layer between the thiolate SAM and the Au surface.

The chemical state and composition of the sample surfaces were analysed by XPS. Typical C 1s, S 2p, and N 1s peaks are shown for the different types of SAM-covered samples in Figure 6.6. The darker colours represent the peaks before Pd clusters were deposited for 60 s, and the lighter colours represent the corresponding values after the deposition. The most important finding from Figure 6.6, is that no major changes can be detected between the substrates before and after Pd cluster deposition, despite the difference between the different samples. There are neither any shifts in the binding energies for the elements detected. Thereby it can be assumed that only weak van der Waals type bonding occur between the Pd clusters and thiolate SAMs.

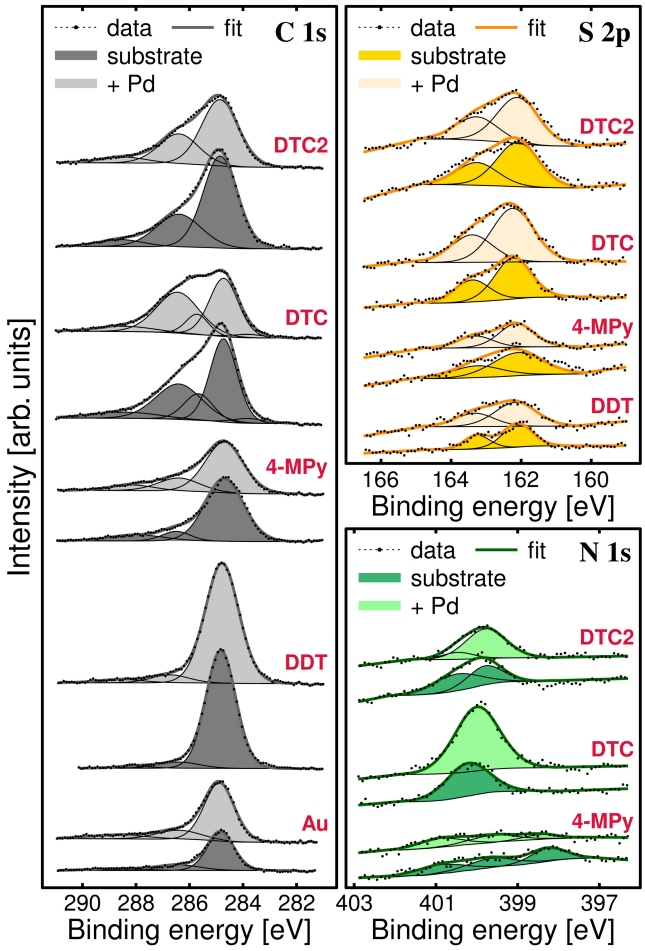

Figure 6.6: High-resolution XPS peaks of C 1s, S 2p, and N 1s core-levels, for bare Au and organic SAM-covered surfaces, both before (darker colours) and after (lighter colours) 60 s Pd cluster deposition. No major shifts in binding energy can be seen for samples before and after deposition [14].

Figure 6.7 shows the relative amount of each element as a function of Pd cluster deposition time for the different types of samples. For the bare Au surface, the relative amount of Au decreases with increasing amount of Pd. There is also an increase in the relative amount of oxygen coupled with the increase of Pd and a slight increase in the amount of carbon. This is most likely due to the oxidation of the Pd clusters upon introduction to the ambient and the slight increase of carbon stems from impurity carbon that binds to the partially oxidized surface. A similar increase in oxygen can be measured for the other sample types as well. A partial covering of the clusters with organic material is most likely the reason for lower Pd intensities for some substrates. According to this the bonding strength between Pd clusters and thiols is lowest for clusters on 4-MPy, and increases for DDT, DTC and DTC2.

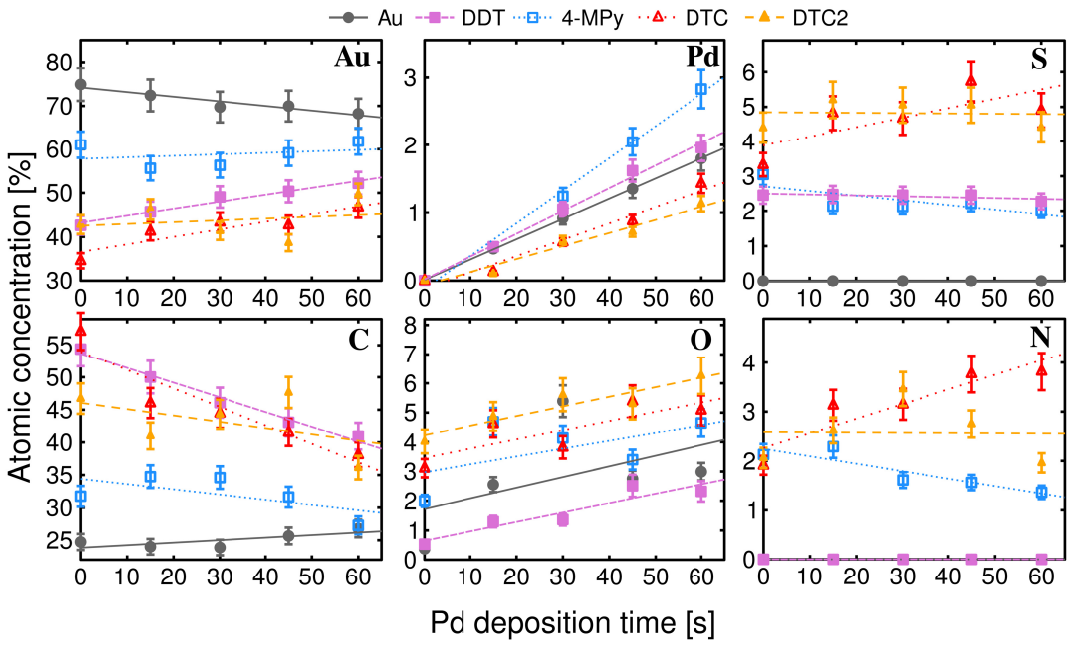

Figure 6.7: The atomic concentrations of elements detected in the samples by XPS. The bare and SAM coated Au(111)surfaces were analysed before and after Pd depositions for 15, 30, 45 and 60 s. Linear fits have been adapted as a first approximation. Error bars represent the combined standard deviation from both peak fitting and measurements on at least three different samples for every substrate type [14].

The relative amount of Au on the SAM covered surfaces increases as the amount of deposited Pd is increased. A possible explanation is that the deposited Pd clusters attract the underlying SAMs so strongly that they agglomerate under the clusters and thereby form higher densities than normally on the Au surface. Since SAM layers typically incorporate several types of intrinsic and extrinsic defects, they can induce lowering in the global density of the organic molecules. This in turn can cause some gold from the substrate to be uncovered, leading to higher intensities of the Au 4f peak. The lowering of the density of organic molecules would explain the unproportionally large decrease in the total carbon concentration.

Figure 6.8 shows the relative ratios between XPS intensities for a) Pd and S, b) Pd and N and c) N and S measured at different photoelectron angles. From a) and b) it can be seen that the relative strength of the Pd signal increases as compared to both S and N signals. This indicates that the Pd clusters are situated above the organic SAM layers, whereas the increased relative amount of N compared to S indicates that the SAM layers have formed a bond to the gold substrate via sulphur and that the nitrogen is facing the ambient.

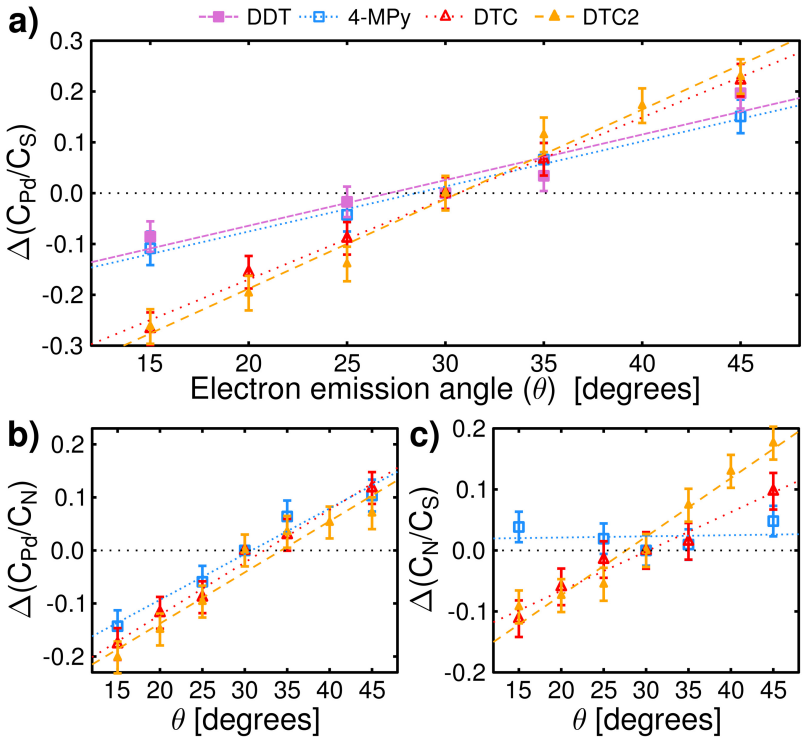

Figure 6.8: Changes in the relative ratios between XPS intensities for a) Pd and S, b) Pd and N, and c) N and S when measured at different photoelectron emission angles. The vertical axes indicate the relative changes in the ratios between the elements, as compared to those measured at an angle of 30°[14].

6.3 Magnetic properties at the nanoscale

6.3.1 Gold

In publication **III** the ferromagnetism of Au cluster agglomerates was studied. As presented in section 4.1 the magnetic phenomena are extremely sensitive to the atomic environment, which is why the magnetic behaviour in assemblies of Au nanoclusters is of interest. In literature data can be found regarding ferro- and superparamagnetic behaviour of Au thin films and individual clusters. Our group has previously studied the ferromagnetism in nanocrystalline gold thin films [86]. The intrinsic magnetic moment of 4 nm bare face-centered cubic (fcc) Au nanoparticles have been investigated by Li et al. [87, 88]. Sato et al. have studied the impact of air exposure of Au nanoclusters in regard of their magnetization as well as the temperature dependence of Au nanocluster magnetization [89, 90]. Studies regarding the size- and temperature dependent structural transitions in gold nanoparticles have

been made by Koga et.al. [91], but not in the connection with their magnetic properties. Consequently experimental studies of the behaviour of similar systems are desirable.

In publication **III** different amounts of Au clusters were deposited (energy 0.3 eV/atom) directly on a template for the SQUID measurements and on carbon holey films for HR-TEM measurements. HR-TEM and AFM were used to determine the size distribution and the developed morphology of the deposited clusters. Table 6.1 summarises the total volume of Au confined in the three different samples used for magnetization measurements. Figure 6.9 demonstrates the developed morphology of our samples. The morphology is a result of unavoidable coalescence and coarsening of the deposited clusters. The 1 min deposition produces a dispersion of separate Au particles, whereas the 20 min deposition results in a fragmentary morphology of gold aggregates that are partly interconnected.

Table 6.1: Summary of the samples showing the total volume of Au confined in them and the deposition time.

sample	symbol	deposition time (min)	volume 10^{-8} (cm^3)
		1	2.5 ± 0.6
A	▲	5	13 ± 3
B	■	10	25 ± 6
C	●	20	50 ± 11

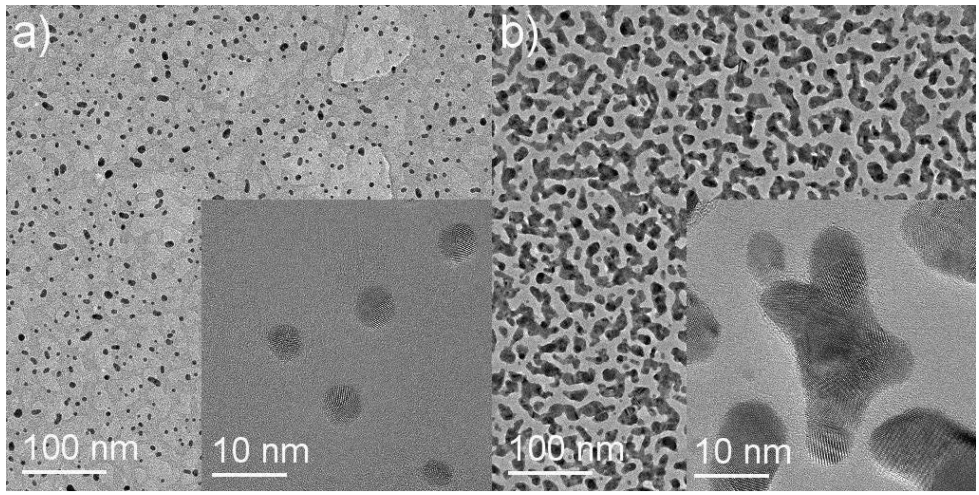

Figure 6.9: HR-TEM micrographs of (a) single Au clusters after 1 min deposition and (b) cluster-assembled aggregates after 20 min deposition (sample C) [92].

Magnetization measurements were performed on all samples (Table 6.1), but no magnetic signal could be detected after 1 min deposition. The magnetization of the deposited nanoparticle samples are shown in Figure 6.10.

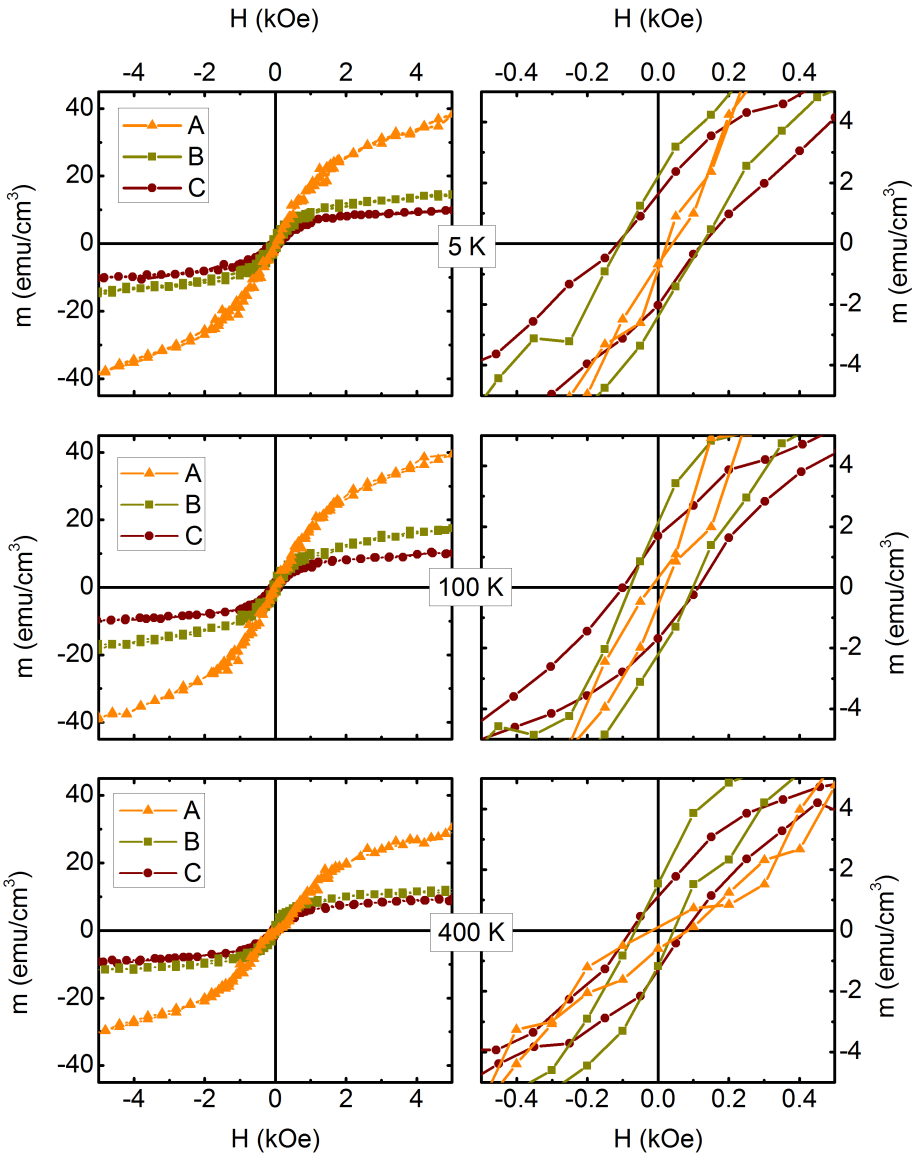

Figure 6.10: Magnetization as a function of magnetic field measured at 5 K, 100 K and 400 K [92].

For samples B and C the magnetization can be seen to exhibit characteristic ferromagnetic hysteresis, with the remanent (M_R) and saturation (M_S) magnetizations, with minor temperature dependence (Figure 6.11). As expected the coercivity (H_C) for samples B and C decreases as a function of temperature, due to thermal excitations. The magnetization of sample A exhibits a typical Langevin function like behaviour, i.e. behaviour characteristic for superparamagnetic (SPM) material. This however is not unexpected as it is a typical behaviour for small interacting ferromagnetic element clusters [93].

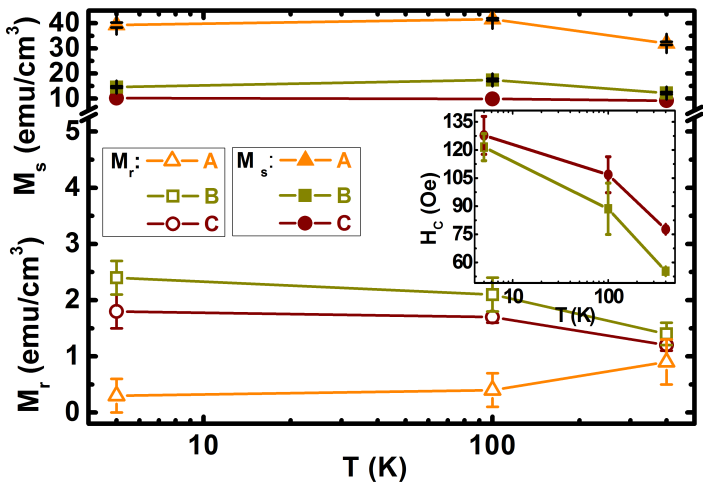

Figure 6.11: Saturation, remanence and coercivity as a function of temperature [92].

Temperature dependence of magnetizationa is presented in Figure 6.12.The measured magnetization can be seen to be irreversible between zero field cooled (ZFC) and field cooled (FC) branches in all of the applied fields. In the case of sample A the Au clusters exhibit typical Langevin type of superparamagnetic core-shell behaviour up to a dilute/percolation limit. As the sample is heated and the clusters connect with one and other the magnetization decreases. Due to the coalescence, dipole and exchange interaction will start to disturb the internal core-valence spin interaction of isolated clusters. The two peaks in the ZFC magnetization are related to the changing interaction between clusters. The narrow low temperature peak between 2 and 4 K is related to surface spin alignment, whereas the broad peak at higher temperature is due to the core-shell spins. The width of the maximum is associated to a wide size distribution among clusters and the corresponding (blocking) energy landscape [94, 95]. In sample B some of the clusters are connected while others still remain isolated, which is why the sample presents a combination of ferromagnetic and Langevin types of interactions. As the cluster density in sample C exceeds the dilute/percolation limit, the sample exhibits saturated ferromagnetic response. The smaller low temperature peak that can be distinguished for samples A and B is due to the core shell/super spin alignment.

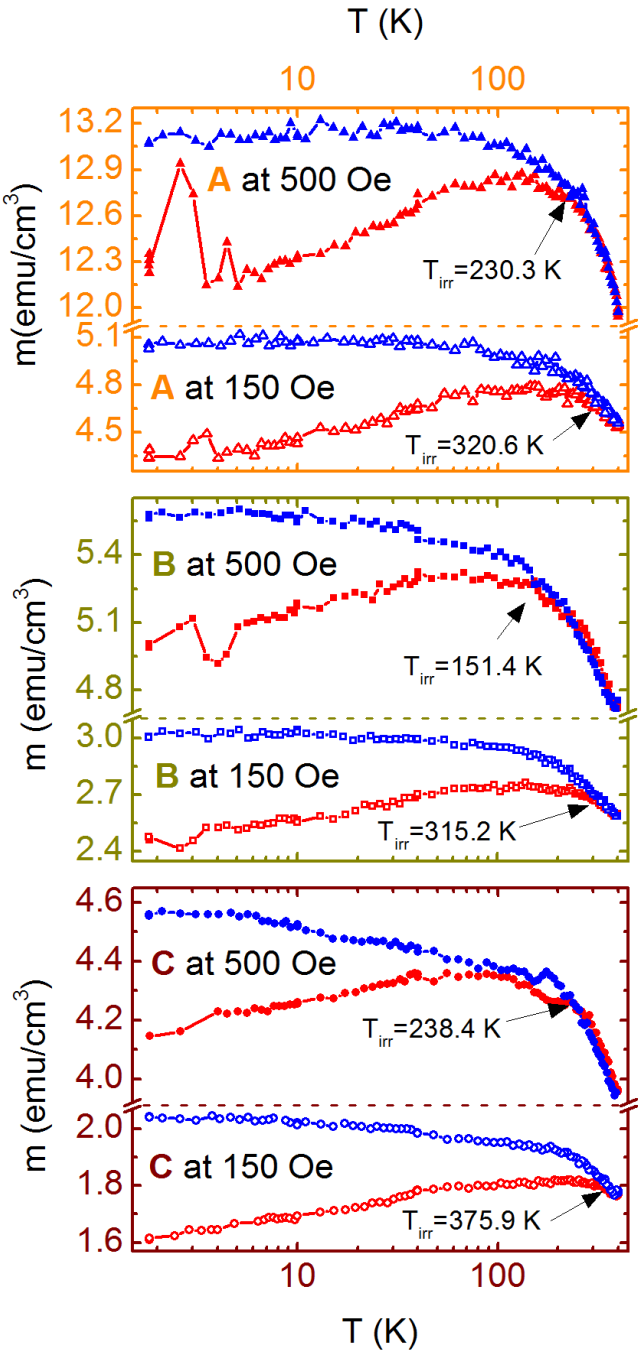

Figure 6.12: Temperature dependence of magnetization in magnetic fields of 150 and 500 Oe. Zero field cooled (ZFC) magnetization in red and field cooled (FC) magnetization in blue [92].

6.3.2 Palladium

For publication **IV** the magnetic behaviour of Pd nanoclusters was investigated by varying the range and degree of interactions of the clusters. Ferromagnetic behaviour in bare Pd fine particles was first reported in 1997 by Tanyama et al. [96], since then similar findings have been reported by others as well [96–106]. The explanation for the occurrence of magnetism at the nanoscale in otherwise nonmagnetic materials however still remain unanswered. Unstable surface atoms in the top few atomic layers in (100) facets are believed to be the origin for the magnetism in nanosized particles [96–98]. According to different theoretical reports available, the ferromagnetism in Pd could arise due to icosahedral structure [107], crystal defects [108], HCP crystal structures [108], surface effects [108] or lattice expansions [109, 110]. Even if the reason for the magnetic behaviour remains unanswered, there seems to be a clear correlation between the ferromagnetic property of Pd at the nanoscale and prevailing defects [111]. As the magnetic phenomena in Pd nanoparticles is highly influenced by the atomic environment, we have chosen to investigate the changes in the magnetic behaviour of Pd nanoclusters, due to changes in degree and range of interactions.

The volume of Pd deposited for publication **IV** was based on rigorous analysis of HR-TEM micrographs, similar to those in Figure 6.13. By varying the deposition time the volume of the Pd confined in the analysed samples could be adjusted. Four different samples with different volumes of Pd were analysed, see Table 6.2. From Figure 6.13 it can be seen that after a 15-min deposition a percolating

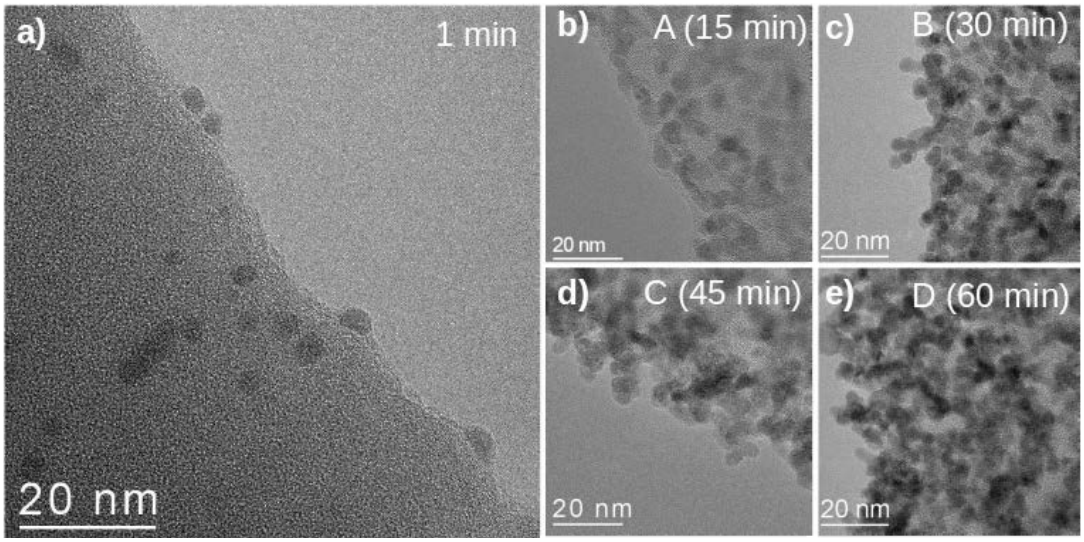

Figure 6.13: HR-TEM micrographs of a) single Pd clusters by a 1-min deposition, b) a percolating network of clusters after a 15-min deposition, c) island growth after a 30-min deposition and the formation of a thin film after a d) 45-min and e) 60-min deposition.

Table 6.2: Summary of the samples showing the total volume of Pd confined in them and the deposition time.

sample	symbol	deposition time (min)	volume 10^{-8} (cm^3)
		1	1.5 ± 0.3
A (A.1/A.2)	□/■	15	23 ± 5
B (B.1/B.2)	○/●	30	45 ± 10
C (C.1/C.2)	△/▲	45	68 ± 15
D (D.1/D.2)	◇/◆	60	90 ± 21

monolayer of Pd clusters has formed. After a 30-min deposition a change to island growth is clear, which in turn leads to surface coarsening. A 60-min deposition results in a porous film, consisting of a network of percolating Pd clusters.

Magnetization measurements were performed on all samples (Table 6.2), but no magnetic signal could be obtained after the 1 min deposition. The acquired magnetization for the samples as function of magnetic field is shown in Figure 6.14. Based on the hysteretic behaviour observed in the M-H curves there is a ferromagnetic spin ordering in the samples. The magnetization curves consist of a saturated ferromagnetic and a paramagnetic component, which implies to the coexistence of ferromagnetism and superparamagnetism in the Pd-cluster films [97, 102]. The proportion of superparamagnetic nanoclusters present in the films is related to the variations in the hysteresis loops [112]. Volume magnetizations, coercivity and remanence were extracted from the M-H curves at temperatures ranging from 1.8 K to 400 K, and are presented in Table 6.3.

Table 6.3: Summary of the results.

Pd form	nanoparticle diameter (nm)	oxidation	T (K)	$\mu_S \cdot 10^{-3}$ (μ_B/atom)	M_S (emu/cm^3)	M_R (emu/cm^3)	H_C (Oe)
NP agglomerates prepared by gas evaporation	4.1 ± 1.6	exposed to ambient conditions					
	$V_A = 2.3 \pm 0.5$		1.8	74 ± 15	46 ± 10	3.4 ± 2.4	85 ± 21
			400	65 ± 6	42 ± 4	2.2 ± 2.1 (300 K)	48 ± 4 (300 K)
	$V_B = 4.5 \pm 1.0$		1.8	26 ± 10	16 ± 6	2.9 ± 0	150 ± 23
			400	22 ± 5	14 ± 4	0.8 ± 0.3	42 ± 3
	$V_C = 6.6 \pm 1.5$		1.8	39 ± 17	24 ± 11	1.5 *	140 *
			400	37 ± 21	23 ± 13	0.48 *	63 *
	$V_D = 9.0 \pm 2.1$		1.8	34 ± 2	22 ± 1	1.3 ± 0.4	68 ± 3
			400	23 ± 6	15 ± 4	0.65 ± 0.16	33 ± 1

* only C.1.

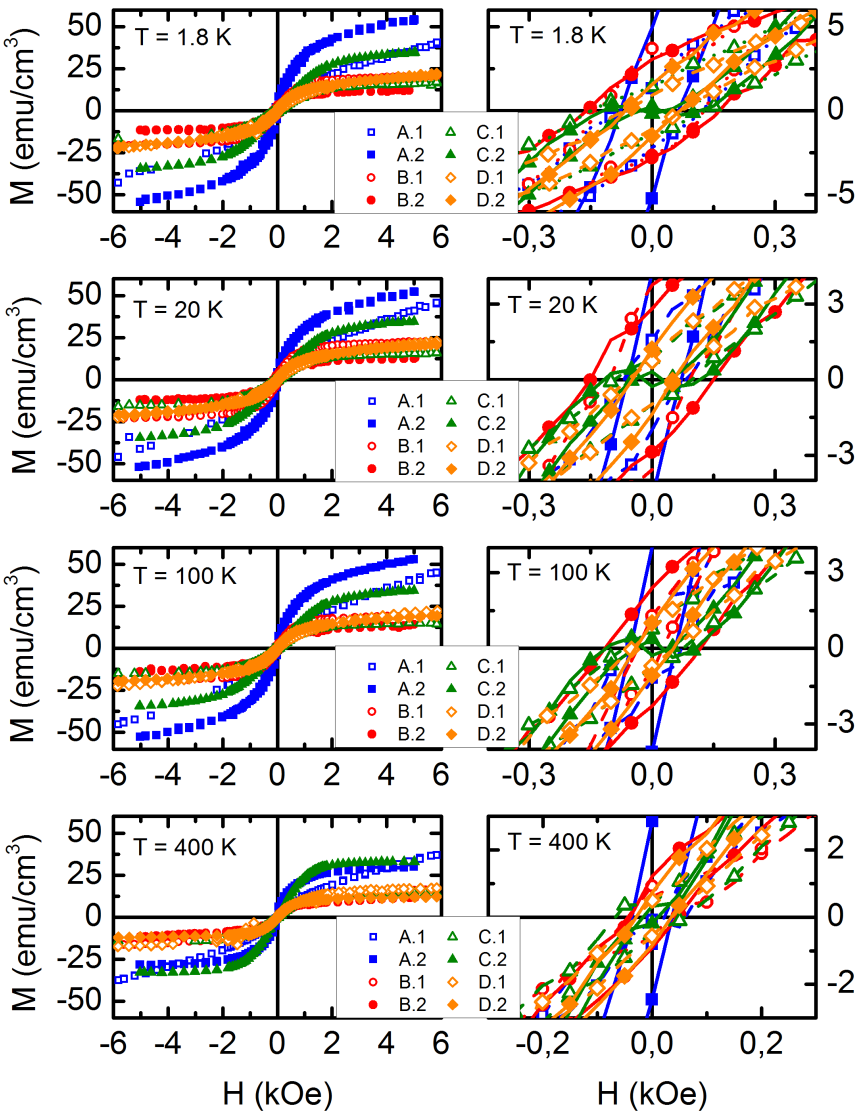

Figure 6.14: Magnetization as a function of magnetic field measured at 1.8 K, 20 K, 100 K and 400 K. In the left column the full range measurements of all of the samples at a given temperature are shown. In the right column zoomed graphs highlighting the remanence and coercivity are shown [113].

Additional information regarding superparamagnetic (SP) and single (SD) (ferro)magnetism of the deposited cluster films was acquired by analysing the data in Figure 6.14 [112]. The difference between the descending and ascending parts of the hysteresis (ΔM) and its derivatives d/dH [ΔM] are shown in Figure 6.15. The shape of the ΔM plots are due to different kinds of hysteresis. For the 15 min deposition the shape of ΔM is due to ”wasp-waist”- hysteresis, where as the d/dH [ΔM] plot (Figure 6.15 e)), corresponds to SD+SP magnetism with two sets of coercivities.

The shape of the ΔM plot for the 30 min deposition (Fig.6.15 b)) shows a combination of "potbelly"- and "wasp-waist"-types of behaviour [112]. The evolving hysteresis from "wasp-waist" to "potbelly" shape is due to an increase of small magnetic clusters with respect to the larger ones found in the 15 min deposition. The ΔM plot for the 45 min deposition is characteristic for a "potbellied" hysteresis (Figure6.15 c)), this indicates that small magnetic clusters dominate and suppress the "wasp-waist" part (in comparison to the 30 min deposition). The merging of the first and second peak in the $\mathrm{d}/\mathrm{d}H\,[\Delta M]$ plot (Fig.6.15 d)) for the 60 min deposition corresponds to the tendency of SP clusters, with single valued coercivity, to transform to a single domain magnetization.

Based on the acquired results we propose that the magnetization of Pd cluster networks and films depends on the growth properties determining the variations in the Pd cluster structures and resulting film morphologies. After a 15 min deposition (initial formation of a film) the coercivity values (by $\mathrm{d}/\mathrm{d}H\,[\Delta M]$) are related to two possible cluster agglomeration configurations: cluster layers and layers with small pile-ups of clusters (islands), which can be seen in the HR-TEM micrographs (Fig.6.13). As the clusters have been deposited for 30 min the magnetization weakens, and can be understood by the reduced surface- to -volume ratio. With an increased amount of Pd clusters on the surface the film growth becomes more complex. The incoming clusters will gain an increased impact energy due to adhesion acceleration, which in turn depends on the impact area between the cluster and the surface [114]. In case of full coalescence of nanoclusters on a Pd substrate, a significant surface energy release will lead to an additional heating of the merging Pd clusters.

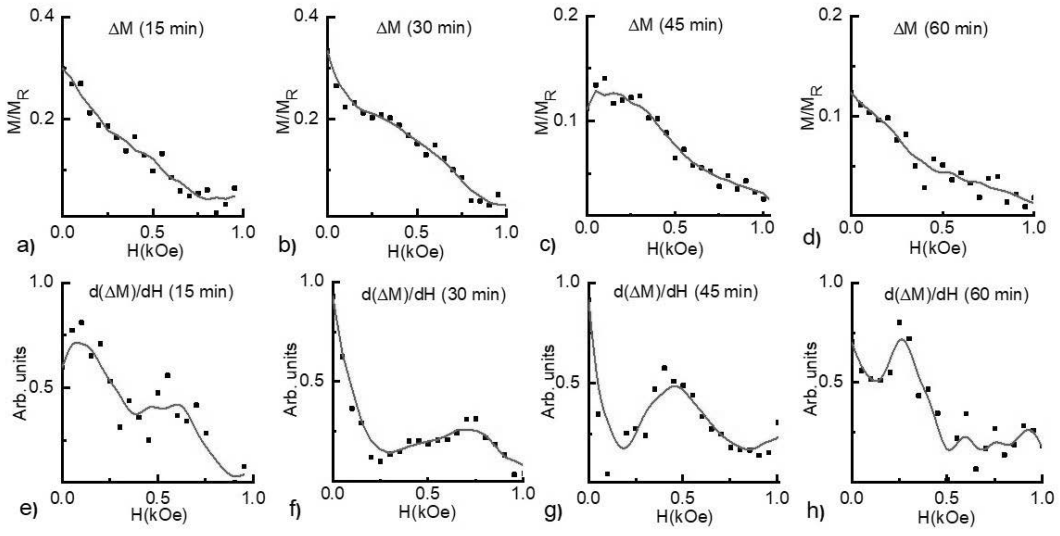

Figure 6.15: The ΔM and its derivative $\mathrm{d}/\mathrm{d}H\,[\Delta M]$ measured at 20 K. The lines in the figure correspond to 5-point averaging of the data [113].

Chapter 7

Conclusions and outlook

The purpose of this study was to contribute to the better understanding of properties related to SAM covered surfaces and the research on the magnetic properties of palladium and gold at the nanoscale. Surfaces covered by SAMs were studied by investigating the morphological changes induced by Ar ion irradiation in bare and thiol functionalized Au(111), as well as the possible metallization of SAM covered surfaces by preformed Pd cluster deposition. Magnetic properties of nanosized Pd and Au were investigated by studying the ferromagnetism in bare Au and Pd nanoagglomerates produced by nanocluster deposition.

Based on our results we can conclude that DDT covered surfaces were more susceptible for irradiation-induced surface morphology changes than the unmodified Au surfaces. Flame-annealing of a Au(111) surface prior to ion bombardment was also found to make it more susceptible to irradiation-induced surface defects. Our results also strongly point toward SAMs of DDT, 4-MPy, DTC, and DTC2 being impenetrable for Pd clusters deposited at thermal energies. Contrary to most methods of metallization, cluster deposition therefore efficiently allows for the growth of metal overlayers on organic SAMs, without the formation of metallic shorts or unwanted interfacial layers. Deposition of preformed metal clusters efficiently hinders the penetration of metal adatoms through the thiolate layers, as all deposited atoms are bound to the clusters, thereby limiting their ability to diffuse on the surface and leak through defects or other parts of the film.

For assemblies of bare gold nanoclusters we presented ferro- and superparamagnetic behaviour dependent on the interactions between particles. The enhanced surface-to-volume atomic ratio was found to favour ferromagnetism in the case of bare Au nanoparticles. The behaviour of the Au cluster agglomerates was also found to be analogous to that of transition metal clusters. For palladium nanocluster thin films we found that the ferromagnetic behaviour is highly dependent on the growth mode and film thickness, as these cause variations in the Pd cluster structures and resulting film morphologies. The surprising magnetism in gold and palladium nanostructures is everything but clear, it opens many new possibilities as well as challenges, before a full understanding of the physical and chemical effects giving rise to this phenomenon is fully understood. These new findings, may open new industrial possibilities towards the design of new functional materials and consequently applications in the field of catalysis, biomedicine and information technology [8].

Acknowledgements

I wish to thank the Department of Physics at the University of Helsinki, for giving me the opportunity to work at at the Accelerator Laboratory and for providing the facilities for the research presented in this thesis. The Doctoral Programme in Material Research and Nanoscience (MATRENA) is gratefully acknowledged for the funding.

First and foremost, I would like to thank my supervisor Prof. *Jyrki Räisänen*, for believing in me and always having time for me. I thank my second supervisor Dr. *Vladimir Tuboltsev*, for the guidance and introducing me to the world of nanoclusters. I'm immensely thankful for all the help and guidance Dr. *Pasi Jalkanen* has provided me with in understanding nanomagnetism. I'm also grateful for the collaboration with Dr. *Minna Räisänen*, who has guided me in the field of self-assembled monolayers. Many thanks are also due to Dr. *Kenichiro Mizohata*, for the ion-irradiations and EDRA-measurements. I also want to thank my co-authors Dr. *Benoît Marchand* and Dr. *Alexandre Savin*. A big thank is also due to Dr. *Kristoffer Meinander*, who after returning to the lab has been one of my supervisors and helped tie all the lose strings together.

I would also want to thank Prof. *Kai Nordlund* for first interviewing me for a position as a summer student at the lab and getting me involved in various work-groups and boards, which have given me great experience in the administrative side of things. I especially want to thank Prof. *Kai Nordlund* and Prof. *Jyrki Räisänen* for letting me evolve in the role as a teacher, giving me the opportunity of taking on more teaching duties than required, lecturing and working as a resource person in physics for *skolresurs.fi*.

The time at the lab would not have been as fun as it has without my present and past collegues. Thank you for all the parties, coffee breaks, more or less insightful discussions, and many many laughs. I especially want to thank my past and current room-mates *Muhammad, Konstantin, Aleksi, Christoffer, Aki*, and *Emil*. I also want to thank the technical personnel who have always helped me whether I have needed liquid nitrogen, had problems with getting my school experiments working, or just needed help with something else. A very special thank goes to my "work-hubby" *Fredric Granberg* for being there, for discussions, support, lunches, and help in various projects both work related and private. I don't know what I would have done without you.

Big thanks goes to my teachers starting from elementary school *Anders Johansson*, for encouraging my interest in mathematics, *Ingvar Stål* at secondary school, for introducing me to physics and to *Leif Ekrem* in upper secondary school for inspiring me and encouraging my interest in science.

I am grateful for all the friends and people I have gotten to know during my studies and time at *Spektrum*. I want to thank my "tanter" *Annika, Henrika, Maria, Sandra and Sonja*, for the friendship and support, and *Nicke* for offering a second living-room and countless dinners. I also want to thank my family for always believing in me. Finally I want to thank *Kristian* for the endless love and support you have given me through this time.

Helsingfors, 24^{th} of November 2018
Annika Venäläinen

References

[1] J. C. Love, L. A. Estroff, J. K. Kriebel, R. G. Nuzzo, and G. M. Whitesides, "Self-assembled monolayers of thiolates on metals as a form of nanotechnology.," *Chem. Rev.*, vol. 105, pp. 1103–69, apr 2005.

[2] G. Schmid and D. Fenske, "Metal clusters and nanoparticles," *Philos. Trans. A. Math. Phys. Eng. Sci.*, vol. 368, pp. 1207–1210, mar 2010.

[3] J. P. Wilcoxon and B. L. Abrams, "Synthesis, structure and properties of metal nanoclusters.," *Chem. Soc. Rev.*, vol. 35, pp. 1162–94, nov 2006.

[4] I. Freestone, N. Meeks, M. Sax, and C. Higgitt, "The Lycurgus Cup — A Roman nanotechnology," *Gold Bull.*, vol. 40, pp. 270–277, dec 2007.

[5] D. J. Barber and I. C. Freestone, "An investigation of the origin of the colour of the Lycurgus Cup by analytical TEM," *Archaeometry*, vol. 32, pp. 33–45, feb 1990.

[6] R. L. Johnston, *Atomic & Molecular Clusters*. CRC Press, 2002.

[7] A. Edelstein and R. Cammaratra, eds., *Nanomaterials: Synthesis, Properties and Applications*. CRC Press, second ed., 1998.

[8] S. Trudel, "Unexpected magnetism in gold nanostructures: making gold even more attractive," *Gold Bull.*, vol. 44, pp. 3–13, feb 2011.

[9] V. N. Popok, I. Barke, E. E. B. Campbell, and K.-H. Meiwes-Broer, "Cluster–surface interaction: From soft landing to implantation," *Surf. Sci. Rep.*, vol. 66, pp. 347–377, oct 2011.

[10] C. P. Poole, F. J. Jones, and F. J. Owens, *Introduction to Nanotechnology*. John Wiley & Sons, Inc., 2003.

[11] J. van Lith, A. Lassesson, S. A. Brown, M. Schulze, J. G. Partridge, and A. Ayesh, "A hydrogen sensor based on tunneling between palladium clusters," *Appl. Phys. Lett.*, vol. 91, p. 181910, oct 2007.

[12] R. Wsuurschum, K. Reimann, S. Grub, A. Ksuubler, P. Scharwaechter, W. Frank, O. Kruse, H. D. Carstanjen, and H.-E. Schaefer, "Structure and diffusional properties of nanocrystalline Pd," *Philos. Mag. Part B*, vol. 76, pp. 407–417, oct 1997.

[13] A. Ulman, "Formation and Structure of Self-Assembled Monolayers.," *Chem. Rev.*, vol. 96, pp. 1533–1554, jun 1996.

[14] A. Venäläinen, K. Meinander, M. Räisänen, V. Tuboltsev, and J. Räisänen, "Metallization of self-assembled organic monolayer surfaces by Pd nanocluster deposition," *Surf. Sci.*, vol. 677, pp. 68–77, nov 2018.

[15] C. D. Bain and G. M. Whitesides, "Attenuation lengths of photoelectrons in hydrocarbon films," *J. Phys. Chem.*, vol. 93, pp. 1670–1673, feb 1989.

[16] P. E. Laibinis, G. M. Whitesides, and D. L. Allara, "Comparison of the Structures and Wetting Properties of Self-Assembled Monolayers of n- Alkanethiols on the Coinage Metal Surfaces, Cu, Ag, Au," *J. Am. Chem. Soc.*, vol. 113, pp. 7152–7167, 1991.

[17] C. Vericat, M. E. Vela, and R. C. Salvarezza, "Self-assembled monolayers of alkanethiols on Au(111): surface structures, defects and dynamics.," *Phys. Chem. Chem. Phys.*, vol. 7, pp. 3258–68, sep 2005.

[18] J. M. Wessels, H.-G. Nothofer, W. E. Ford, F. von Wrochem, F. Scholz, T. Vossmeyer, A. Schroedter, H. Weller, and A. Yasuda, "Optical and Electrical Properties of Three-Dimensional Interlinked Gold Nanoparticle Assemblies," *J. Am. Chem. Soc.*, vol. 126, pp. 3349–3356, mar 2004.

[19] Y. Zhao, W. Pérez-Segarra, Q. Shi, and A. Wei, "Dithiocarbamate Assembly on Gold," *J. Am. Chem. Soc.*, vol. 127, pp. 7328–7329, may 2005.

[20] P. Morf, F. Raimondi, H.-G. Nothofer, B. Schnyder, A. Yasuda, J. M. Wessels, and T. A. Jung, "Dithiocarbamates: Functional and Versatile Linkers for the Formation of Self-Assembled Monolayers," *Langmuir*, vol. 22, pp. 658–663, jan 2006.

[21] H. Zhu, D. M. Coleman, C. J. Dehen, I. M. Geisler, D. Zemlyanov, J. Chmielewski, G. J. Simpson, and A. Wei, "Assembly of Dithiocarbamate-Anchored Monolayers on Gold Surfaces in Aqueous Solutions," *Langmuir*, vol. 24, pp. 8660–8666, aug 2008.

[22] Z. Li and D. S. Kosov, "Dithiocarbamate Anchoring in Molecular Wire Junctions: A First Principles Study," *J. Phys. Chem. B*, vol. 110, pp. 9893–9898, may 2006.

[23] M. Saitner, F. Eberle, J. Baccus, M. D'Olieslaeger, P. Wagner, D. M. Kolb, and H.-G. Boyen, "Impact of Functional Groups onto the Electronic Structure of Metal Electrodes in Molecular Junctions," *J. Phys. Chem. C*, vol. 116, pp. 21810–21815, oct 2012.

[24] F. Eberle, M. Saitner, H.-G. Boyen, J. Kucera, A. Gross, A. Romanyuk, P. Oelhafen, M. D'Olieslaeger, M. Manolova, and D. M. Kolb, "A Molecular Double Decker: Extending the Limits of Current Metal-Molecule Hybrid Structures," *Angew. Chemie Int. Ed.*, vol. 49, pp. 341–345, jan 2010.

[25] M. Manolova, H.-G. Boyen, J. Kucera, A. Groß, A. Romanyuk, P. Oelhafen, V. Ivanova, and D. M. Kolb, "Chemical Interactions at Metal/Molecule Interfaces in Molecular Junctions-A Pathway Towards Molecular Recognition," *Adv. Mater.*, vol. 21, pp. 320–324, jan 2009.

[26] H.-G. Boyen, P. Ziemann, U. Wiedwald, V. Ivanova, D. M. Kolb, S. Sakong, A. Gross, A. Romanyuk, M. Büttner, and P. Oelhafen, "Local density of states effects at the metal-molecule interfaces in a molecular device," *Nat. Mater.*, vol. 5, pp. 394–399, may 2006.

[27] O. Shekhah, C. Busse, A. Bashir, F. Turcu, X. Yin, P. Cyganik, A. Birkner, W. Schuhmann, and C. Wöll, "Electrochemically deposited Pd islands on an organic surface: the presence of Coulomb blockade in STM I(V) curves at room temperature.," *Phys. Chem. Chem. Phys.*, vol. 8, pp. 3375–8, aug 2006.

[28] J. Kučera and A. Groß, "Reduced Pd density of states in Pd/SAM/Au junctions: the role of adsorbed hydrogen atoms," *Phys. Chem. Chem. Phys.*, vol. 14, no. 7, p. 2353, 2012.

[29] T. Baunach, V. Ivanova, D. M. Kolb, H.-G. Boyen, P. Ziemann, M. Büttner, and P. Oelhafen, "A New Approach to the Electrochemical Metallization of Organic Monolayers: Palladium Deposition onto a 4,4?-Dithiodipyridine Self-Assembled Monolayer," *Adv. Mater.*, vol. 16, pp. 2024–2028, nov 2004.

[30] V. Ivanova, T. Baunach, and D. M. Kolb, "Metal deposition onto a thiol-covered gold surface: A new approach," *Electrochim. Acta*, vol. 50, pp. 4283–4288, aug 2005.

[31] M. Manolova, V. Ivanova, D. Kolb, H.-G. Boyen, P. Ziemann, M. Büttner, A. Romanyuk, and P. Oelhafen, "Metal deposition onto thiol-covered gold: Platinum on a 4-mercaptopyridine SAM," *Surf. Sci.*, vol. 590, pp. 146–153, oct 2005.

[32] W. Harbich, "Collision of Clusters with Surfaces: Deposition, Surface Modification and Scattering," in *Met. Clust. Surfaces Struct. Quantum Prop. Phys. Chem.* (K.-H. Meiwes-Broer, ed.), ch. 4, pp. 107–150, Berlin, Heidelberg: Springer Berlin Heidelberg, 2000.

[33] A. M. Bittner, "Clusters on soft matter surfaces," *Surf. Sci. Rep.*, vol. 61, pp. 383–428, nov 2006.

[34] C. Binns, "Nanoclusters deposited on surfaces," *Surf. Sci. Rep.*, vol. 44, no. 1-2, pp. 1–49, 2001.

[35] W. D. J. Callister and D. G. Rethwish, *Fundamentals of Materials Science and Engineering*. John Wiley & Sons Ltd, 4th ed., 2013.

[36] A. Kolhatkar, A. Jamison, D. Litvinov, R. Willson, and T. Lee, "Tuning the Magnetic Properties of Nanoparticles," *Int. J. Mol. Sci.*, vol. 14, pp. 15977–16009, jul 2013.

[37] S. Bedanta, O. Petracic, and W. Kleemann, "Supermagnetism," in *Handb. Magn. Mater.* (K. H. J. Buschow, ed.), ch. Chapter 1, pp. 1–83, Elsevier, 2015.

[38] G. C. Papaefthymiou, "Nanoparticle magnetism," *Nano Today*, vol. 4, pp. 438–447, oct 2009.

[39] B. Issa, I. Obaidat, B. Albiss, and Y. Haik, "Magnetic Nanoparticles: Surface Effects and Properties Related to Biomedicine Applications," *Int. J. Mol. Sci.*, vol. 14, pp. 21266–21305, oct 2013.

[40] J. L. Dormann, D. Fiorani, and E. Tronc, "Magnetic Relaxation in Fine-Particle Systems," in *Adv. Chem. Phys.* (I. Prigogine and S. A. Rice, eds.), ch. 4, pp. 283–494, John Wiley & Sons, Inc., mar 2007.

[41] E. Coronado, B. S. Tsukerblat, and R. Georges, *Exchange Interactions I: Mechanisms*, pp. 65–84. Dordrecht: Springer Netherlands, 1996.

[42] S. Mørup and M. F. Hansen, "Superparamagnetic Particles," in *Handb. Magn. Adv. Magn. Mater.*, Chichester, UK: John Wiley & Sons, Ltd, dec 2007.

[43] J. Sung Lee, J. Myung Cha, H. Young Yoon, J.-K. Lee, and Y. Keun Kim, "Magnetic multi-granule nanoclusters: A model system that exhibits universal size effect of magnetic coercivity," *Sci. Rep.*, vol. 5, p. 12135, dec 2015.

[44] E. F. Kneller and F. E. Luborsky, "Particle Size Dependence of Coercivity and Remanence of Single-Domain Particles," *J. Appl. Phys.*, vol. 34, pp. 656–658, mar 1963.

[45] M. J. Bonder, Y. Huang, and G. C. Hadjipanayis, *Magnetic Nanoparticles*, pp. 183–206. Boston: Kluwer Academic Publishers, 2006.

[46] M. Hansen and S. Mørup, "Estimation of blocking temperatures from ZFC/FC curves," *J. Magn. Magn. Mater.*, vol. 203, pp. 214–216, aug 1999.

[47] Y. Yamamoto, T. Miura, M. Suzuki, N. Kawamura, H. Miyagawa, T. Nakamura, K. Kobayashi, T. Teranishi, and H. Hori, "Direct Observation of Ferromagnetic Spin Polarization in Gold Nanoparticles," *Phys. Rev. Lett.*, vol. 93, p. 116801, sep 2004.

[48] "Oxford Applied Research, Nanocluster Deposition Source-Model NC200U-B."

[49] P. J. Kelly and R. D. Arnell, "Magnetron sputtering: a review of recent developments and applications," *Vacuum*, vol. 56, pp. 159–172, mar 2000.

[50] I. M. Goldby, B. von Issendorff, L. Kuipers, and R. E. Palmer, "Gas condensation source for production and deposition of size-selected metal clusters," *Rev. Sci. Instrum.*, vol. 68, pp. 3327–3334, sep 1997.

[51] H. Haberland, ed., *Clusters of Atoms and Molecules*, vol. 52 of *Springer Series in Chemical Physics*. Berlin, Heidelberg: Springer Berlin Heidelberg, 1994.

[52] I. Yamada and N. Toyoda, "Recent advances in R&D of gas cluster ion beam processes and equipment," *Nucl. Instruments Methods Phys. Res. Sect. B Beam Interact. with Mater. Atoms*, vol. 241, pp. 589–593, dec 2005.

[53] B. Satpati and B. N. Dev, "Replicating Nanostructures on Silicon by Low Energy Ion Beams," *Nanotechnology*, vol. 16, no. 4, p. 12, 2004.

[54] H. Gnaser, "Interaction of low-energy ions with solids," in *Low-Energy Ion Irradiat. Solid Surfaces*, pp. 7–82, Berlin, Heidelberg: Springer Berlin Heidelberg, 1999.

[55] H. Gnaser, "Nanostructures on surfaces by ion irradiation," *Pure Appl. Chem.*, vol. 83, jan 2011.

[56] M. V. Salapaka and S. M. Salapaka, "Scanning Probe Microscopy," *IEEE Control Syst. Mag.*, vol. 28, pp. 65–83, apr 2008.

[57] A. Collins, *Nanotechnology Cookbook: Practical, Reliable And Jargon-Free Experimental Procedures*. United Kingdom: Elsevier Science LTD, 2012.

[58] C. J. Chen, *Introduction to Scanning Tunneling Microscopy (Monographs on the Physics and Chemistry of Materials)*. Oxford University Press, USA, 2007.

[59] P. Klapetek, D. Necas, "Gwyddion," 2014.

[60] L. Reimer, *Transmission Electron Microscopy*, vol. 36 of *Springer Series in Optical Sciences*. Berlin, Heidelberg: Springer Berlin Heidelberg, 1984.

[61] C. C. Chusuei and D. Goodman, "X-Ray Photoelectron Spectroscopy," in *Encycl. Phys. Sci. Technol.*, pp. 921–938, Elsevier, 2003.

[62] J. F. Watts, "X-ray photoelectron spectroscopy," *Vacuum*, vol. 45, pp. 653–671, jun 1994.

[63] D.-Q. Yang, K. N. Piyakis, and E. Sacher, "The manipulation of Cu cluster dimensions on highly oriented pyrolytic graphite surfaces by low energy ion beam irradiation," *Surf. Sci.*, vol. 536, pp. 67–74, jun 2003.

[64] R. L. Fagaly, "Superconducting quantum interference device instruments and applications," *Rev. Sci. Instrum.*, vol. 77, p. 101101, oct 2006.

[65] B. Donnio, J. L. Gallani, and M. V. Rastei, "Characterization of Magnetism in Gold Nanoparticles," in *Magn. Charact. Tech. Nanomater.*, pp. 191–207, Berlin, Heidelberg: Springer Berlin Heidelberg, 2017.

[66] J. Pomeroy, A. Perrella, H. Grube, and J. Gillaspy, "Gold nanostructures created by highly charged ions," *Phys. Rev. B*, vol. 75, p. 241409, jun 2007.

[67] J. Pomeroy, H. Grube, A. Perrella, and J. Gillaspy, "STM and transport measurements of highly charged ion modified materials," *Nucl. Instruments Methods Phys. Res. Sect. B Beam Interact. with Mater. Atoms*, vol. 258, pp. 189–193, may 2007.

[68] F. Aumayr, A. El-Said, and W. Meissl, "Nano-sized surface modifications induced by the impact of slow highly charged ions – A first review," *Nucl. Instruments Methods Phys. Res. Sect. B Beam Interact. with Mater. Atoms*, vol. 266, pp. 2729–2735, jun 2008.

[69] B. Arezki, A. Delcorte, A. Chami, B. Garrison, and P. Bertrand, "Gold-thiolate cluster emission from SAMs under keV ion bombardment: Experiments and molecular dynamics simulations," *Nucl. Instruments Methods Phys. Res. Sect. B Beam Interact. with Mater. Atoms*, vol. 212, pp. 369–375, dec 2003.

[70] B. Arezki, A. Delcorte, B. J. Garrison, and P. Bertrand, "Understanding gold-thiolate cluster emission from self-assembled monolayers upon kiloelectronvolt ion bombardment.," *J. Phys. Chem. B*, vol. 110, pp. 6832–40, apr 2006.

[71] P. Cyganik, Z. Postawa, C. Meserole, E. Vandeweert, and N. Winograd, "Ion-induced erosion of organic self-assembled monolayers," *Nucl. Instruments Methods Phys. Res. Sect. B Beam Interact. with Mater. Atoms*, vol. 148, pp. 137–142, jan 1999.

[72] B. O'Rourke, M. Flores, V. A. Esaulov, Y. Yamazaki, B. E. O'Rourke, M. Flores, V. A. Esaulov, and Y. Yamazaki, "Modification of self assembled monolayers by highly charged ions," *Nucl. Instruments Methods Phys. Res. Sect. B Beam Interact. with Mater. Atoms*, vol. 299, pp. 68–70, mar 2013.

[73] A. Venäläinen, M. T. Räisänen, B. Marchand, K. Mizohata, and J. Räisänen, "Argon ion irradiation induced morphological instability of bare and thiol-functionalized Au(111) surfaces," *Phys. Chem. Chem. Phys.*, vol. 17, no. 16, pp. 10838–10848, 2015.

[74] L. Costelle, T. T. Jarvi, M. T. Raisanen, V. Tuboltsev, and J. Raisanen, "Binding of deposited gold clusters to thiol self-assembled monolayers on Au(111) surfaces," *Appl. Phys. Lett.*, vol. 98, no. 4, p. 043107, 2011.

[75] L. Costelle, M. T. Raisanen, J. T. Joyce, C. Silien, L.-S. Johansson, J. M. Campbell, and J. Raisanen, "Structural Evolution of Gas-Phase Coinage Metal Clusters in Thiolate Self-Assembled Monolayers on Au," *J. Phys. Chem. C*, vol. 116, pp. 22602–22607, oct 2012.

[76] E. A. Speets, P. te Riele, M. A. F. van den Boogaart, L. M. Doeswijk, B. J. Ravoo, G. Rijnders, J. Brugger, D. N. Reinhoudt, and D. H. A. Blank, "Formation of Metal Nano- and Micropatterns on Self-Assembled Monolayers by Pulsed Laser Deposition Through Nanostencils and Electroless Deposition," *Adv. Funct. Mater.*, vol. 16, pp. 1337–1342, jul 2006.

[77] E. A. Speets, B. Dordi, B. J. Ravoo, N. Oncel, A.-S. Hallbäck, H. J. W. Zandvliet, B. Poelsema, G. Rijnders, D. H. A. Blank, and D. N. Reinhoudt, "Noble metal nanoparticles deposited on self-assembled monolayers by pulsed laser deposition show coulomb blockade at room temperature.," *Small*, vol. 1, pp. 395–8, apr 2005.

[78] E. A. Speets, B. J. Ravoo, F. J. G. Roesthuis, F. Vroegindeweij, D. H. A. Blank, and D. N. Reinhoudt, "Fabrication of Arrays of Gold Islands on Self-Assembled Monolayers Using Pulsed Laser Deposition through Nanosieves," *Nano Lett.*, vol. 4, pp. 841–844, may 2004.

[79] C. Winter, U. Weckenmann, R. A. Fischer, . J. Käshammer, V. Scheumann, and S. Mittler, "Selective Nucleation and Area-Selective OMCVD of Gold on Patterned Self-Assembled Organic Monolayers Studied by AFM and XPS: A Comparison of OMCVD and PVD," *Chem. Vap. Depos.*, vol. 6, pp. 199–205, aug 2000.

[80] H. Kind, A. M. Bittner, O. Cavalleri, K. Kern, and T. Greber, "Electroless Deposition of Metal Nanoislands on Aminothiolate-Functionalized Au(111) Electrodes," *J. Phys. Chem. B*, vol. 102, pp. 7582–7589, sep 1998.

[81] F. Camacho-Alanis, L. Wu, G. Zangari, and N. Swami, "Molecular junctions of 1 nm device length on self-assembled monolayer modified n- vs. p-GaAs," *J. Mater. Chem.*, vol. 18, no. 45, p. 5459, 2008.

[82] M. I. Muglali, J. Liu, A. Bashir, D. Borissov, M. Xu, Y. Wang, C. Wöll, and M. Rohwerder, "On the complexation kinetics for metallization of organic layers: palladium onto a pyridine-terminated araliphatic thiol film.," *Phys. Chem. Chem. Phys.*, vol. 14, pp. 4703–12, apr 2012.

[83] P. Morf, N. Ballav, M. Putero, F. von Wrochem, J. M. Wessels, and T. A. Jung, "Supramolecular Structures and Chirality in Dithiocarbamate Self-Assembled Monolayers on Au(111)," *J. Phys. Chem. Lett.*, vol. 1, pp. 813–816, mar 2010.

[84] A. F. Raigoza, G. Kolettis, T. E. S. Brandt, G. Caponigri-Guerra, C. Agostino, and S. A. Kandel, "Coadsorption of Octanethiol and Dialkyldithiocarbamate on Au(111)," *J. Phys. Chem. C*, vol. 116, pp. 1930–1934, jan 2012.

[85] D. Zhang, C. Jin, H. Tian, Y. Xiong, H. Zhang, P. Qiao, J. Fan, Z. Zhang, Z. Y. Li, and J. Li, "An In situ TEM study of the surface oxidation of palladium nanocrystals assisted by electron irradiation," *Nanoscale*, vol. 9, no. 19, pp. 6327–6333, 2017.

[86] V. Tuboltsev, A. Savin, A. Pirojenko, and J. Räisänen, "Magnetism in nanocrystalline gold.," *ACS Nano*, vol. 7, pp. 6691–6699, aug 2013.

[87] F. Li, L. Tang, W. Zhou, and Q. Guo, "Single layer gold islands at the interface between a self-assembled monolayer and the Au(111) substrate: A high-resolution STM study," *Surf. Sci.*, vol. 605, pp. 1016–1020, jun 2011.

[88] C.-M. Wu, C.-Y. Li, Y.-T. Kuo, C.-W. Wang, S.-Y. Wu, and W.-H. Li, "Quantum spins in Mackay icosahedral gold nanoparticles," *J. Nanoparticle Res.*, vol. 12, pp. 177–185, jan 2010.

[89] S. Ishikawa and T. Sato, "Verification of Ferromagnetism in Au Nanoparticles with Clean Surface," in *Proc. 12th Asia Pacific Phys. Conf.*, Journal of the Physical Society of Japan, mar 2014.

[90] R. Sato, S. Ishikawa, H. Sato, and T. Sato, "Magnetic order of Au nanoparticle with clean surface," *J. Magn. Magn. Mater.*, vol. 393, pp. 209–212, nov 2015.

[91] K. Koga, T. Ikeshoji, and K.-i. Sugawara, "Size- and Temperature-Dependent Structural Transitions in Gold Nanoparticles," *Phys. Rev. Lett.*, vol. 92, p. 115507, mar 2004.

[92] A. Venäläinen, P. Jalkanen, V. Tuboltsev, K. Meinander, A. Savin, and J. Räisänen, "Ferromagnetism in bare gold nanoagglomerates produced by nanocluster deposition," *J. Magn. Magn. Mater.*, vol. 454, pp. 57–60, may 2018.

[93] V. Singh and V. Banerjee, "Ferromagnetism, hysteresis and enhanced heat dissipation in assemblies of superparamagnetic nanoparticles," *J. Appl. Phys.*, vol. 112, no. 11, p. 114912, 2012.

[94] L. León Félix, J. A. H. Coaquira, M. A. R. Martínez, G. F. Goya, J. Mantilla, M. H. Sousa, L. d. l. S. Valladares, C. H. W. Barnes, and P. C. Morais, "Structural and magnetic properties of core-shell Au/Fe3O4 nanoparticles," *Sci. Rep.*, vol. 7, p. 41732, feb 2017.

[95] B. Pacakova, S. Kubickova, A. Reznickova, D. Niznansky, and J. Vejpravova, "Spinel Ferrite Nanoparticles: Correlation of Structure and Magnetism," in *Magn. Spinels - Synth. Prop. Appl.*, InTech, mar 2017.

[96] T. Taniyama, E. Ohta, and T. Sato, "Observation of 4d ferromagnetism in free-standing Pd fine particles," *Europhys. Lett.*, vol. 38, no. 3, pp. 195–200, 1997.

[97] T. Shinohara, T. Sato, and T. Taniyama, "Surface ferromagnetism of Pd fine particles.," *Phys. Rev. Lett.*, vol. 91, no. 19, p. 197201, 2003.

[98] Y. T. Jeon and G. H. Lee, "Magnetism of the fcc Rh and Pd nanoparticles," *J. Appl. Phys.*, vol. 103, no. 9, pp. 10–15, 2008.

[99] Y. Oba, H. Okamoto, T. Sato, T. Shinohara, J. Suzuki, T. Nakamura, T. Muro, and H. Osawa, "X-ray magnetic circular dichroism study on ferromagnetic Pd nanoparticles," *J. Phys. D. Appl. Phys.*, vol. 41, no. 13, p. 134024, 2008.

[100] T. Taniyama, E. Ohta, and T. Sato, "Ferromagnetism of Pd fine particles," *Phys. B Condens. Matter*, vol. 237-238, pp. 286–288, jul 1997.

[101] T. Shinohara, T. Sato, and T. Taniyama, "Ferromagnetism of gas-evaporated Pd fine particles in mesoscopic size," *J. Magn. Magn. Mater.*, vol. 272-276, no. SUPPL. 1, pp. 2003–2004, 2004.

[102] Y. Oba, T. Sato, and T. Shinohara, "Gas Adsorption on the Surface of Ferromagnetic Pd Nanoparticles," *e-Journal Surf. Sci. Nanotechnol.*, vol. 4, no. April, pp. 439–442, 2006.

[103] B. Sampedro, T. C. Rojas, a. Fernández, and a. Hernando, "Palladium nanoparticles obtained by mechanical milling," *Phys. Status Solidi*, vol. 203, no. 6, pp. 1201–1205, 2006.

[104] Y. Oba, T. Sato, and T. Shinohara, "Ferromagnetism induced by strains in Pd nanoparticles," *Phys. Rev. B - Condens. Matter Mater. Phys.*, vol. 78, no. 22, pp. 1–5, 2008.

[105] T. Okamoto, H. Maki, Y. Oba, S. Yabuuchi, T. Sato, and E. Ohta, "Electrical detection of ferromagnetism in Pd nanoparticles by magnetoresistance measurement," *J. Appl. Phys.*, vol. 106, no. 2, 2009.

[106] M. S. Seehra, J. D. Rall, J. C. Liu, and C. B. Roberts, "Core-shell model for the magnetic properties of Pd nanoparticles," *Mater. Lett.*, vol. 68, pp. 347–349, 2012.

[107] L. Vitos, B. Johansson, and J. Kollár, "Size-dependent paramagnetic-ferromagnetic phase transition in palladium clusters," *Phys. Rev. B - Condens. Matter Mater. Phys.*, vol. 62, no. 18, pp. 957–960, 2000.

[108] S. S. Alexandre, E. Anglada, J. M. Soler, and F. Yndurain, "Magnetism of two-dimensional defects in Pd: Stacking faults, twin boundaries, and surfaces," *Phys. Rev. B - Condens. Matter Mater. Phys.*, vol. 74, no. 5, pp. 1–7, 2006.

[109] V. L. Moruzzi and P. M. Marcus, "Magnetism in fcc rhodium and palladium," *Phys. Rev. B*, vol. 39, no. 1, pp. 471–474, 1989.

[110] H. Chen, N. Brener, and J. Callaway, "Electronic structure, optical and magnetic properties of fcc palladium," *Phys. Rev. B*, vol. 40, no. 3, pp. 1443–1449, 1989.

[111] P. K. Kulriya, B. R. Mehta, D. C. Agarwal, P. Kumar, S. M. Shivaprasad, J. C. Pivin, and D. K. Avasthi, "Giant enhancement in ferromagnetic properties of Pd nanoparticle induced by intentionally created defects," *J. Appl. Phys.*, vol. 112, no. 1, 2012.

[112] L. Tauxe, T. A. T. Mullender, and T. Pick, "Potbellies, wasp-waists, and superparamagnetism in magnetic hysteresis," *J. Geophys. Res. Solid Earth*, vol. 101, pp. 571–583, jan 1996.

[113] A. Venäläinen, P. Jalkanen, V. Tuboltsev, A. Savin, and J. Räisänen, "Growth mode-dependent ferromagnetic properties of palladium nanoclusters," *J. Appl. Phys.*, vol. 124, p. 033904, jul 2018.

[114] K. Meinander, K. Nordlund, and J. Keinonen, "Inherent surface roughening as a limiting factor in epitaxial cluster deposition," *Nucl. Instruments Methods Phys. Res. Sect. B Beam Interact. with Mater. Atoms*, vol. 228, pp. 69–74, jan 2005.